Advanced Engineering Informatics 72 (2026) 104483

Contents lists available at ScienceDirect

Advanced Engineering Informatics

journal homepage: www.elsevier.com/locate/aei

Full length article

Generative inverse design of steel gridshell joints with multi-objective optimisation

Man-Tai Chen [a,b], Yue Pan [a,b], Wenkang Zuo [c,*], Ou Zhao [d], Leroy Gardner [e]

[a] State Key Laboratory of Ocean Engineering, Shanghai Jiao Tong University, Shanghai 200240, China
[b] Shanghai Key Laboratory for Digital Maintenance of Buildings and Infrastructure, Department of Civil Engineering, Shanghai Jiao Tong University, Shanghai 200240, China
[c] Dept. of Civil and Environmental Engineering, The Hong Kong Polytechnic University, Hong Kong, China
[d] School of Civil and Environmental Engineering, Nanyang Technological University, Singapore
[e] Dept. of Civil and Environmental Engineering, Imperial College London, South Kensington Campus, London SW7 2AZ, UK

A R T I C L E I N F O

Keywords:
Generativedesign
Machine learning
Multi-objective optimisation
Steel joint

A B S T R A C T

The design of steel gridshell joints, simultaneously minimising weight, maximising stiffness and ensuring a uniform stress distribution, is a challenging multi-objective problem. This paper presents a generative inverse design framework integrating topology optimisation (TO), data-driven surrogate modelling and multi-objective optimisation to automatically generate high-performance steel joint designs. A parametric workflow links a BESO-based TO module with a Bayesian-optimised XGBoost surrogate model for predicting joint compliance and stress variation. An NSGA-II parametric evolutionary optimiser then explores trade-offs among competing objectives, while K-means clustering extracts representative Pareto-optimal solutions. The effectiveness of the framework is validated by a case study, with the generated joints achieving up to 40% weight reduction and improved stiffness and stress uniformity relative to a conventional hollow joint. One selected design was successfully fabricated via selective laser melting 3D printing, demonstrating practical manufacturability. The proposed framework is also adaptive to other steel gridshell joint forms.

1. Introduction

Gridshell structures, renowned for their architectural elegance and structural efficiency, have been prominently utilised in landmark projects such as the Sun Valley of the Shanghai Expo Axis in China (Fig. 1(a)) and King's Cross Railway Station in the UK. Central to the construction of steel gridshell structures is the design and manufacture of the joints, which play a critical role in their mechanical performance and overall safety [1–3]. These structures commonly employ a large number of six member-type tubular joints. In practical applications, these joints are typically realised in two configurations: four inclined braces welded to a chord along its longitudinal axis (Fig. 1(b)), or six members welded to a hollow spherical connection (Fig. 1(c)). However, the intersecting regions of joints exhibit low material utilization efficiency, and the chord or hollow sphere often experiences plastic deformation or cracking under complex load [4] (as shown in Fig. 1(b)); hence, additional reinforcement is often required [5–8]. Furthermore, onsite welding of complex joints is labour-intensive and prone to post-welding residual stresses if improperly handled, resulting in elevated stress concentrations. These stress concentrations increase the risk of fatigue damage under cyclic loading [9].

Topology Optimisation (TO), a performance-driven generative design methodology, provides a transformative approach to these challenges by optimising the distribution of material under specific constraints [10,11]. Over the past decade, both academia and industry [12–19] have extensively investigated the application of TO to gridshell joints, consistently demonstrating their superior mechanical and material efficiency. Compared to conventional standardised counterparts, TO designed joints exhibit reduced stress concentrations, more uniform stress distributions, enhanced global stiffness and significantly improved material utilization [16]. Moreover, these designs harmoniously integrate aesthetics with mechanical performance. Metal 3D printing [20–25], or additive manufacturing (AM), as a cutting-edge manufacturing technology, facilitates the production of these geometrically complex TO solutions.

Ensuring reliable mechanical performance is crucial for the safe

---

* Corresponding author.
E-mail address: zuowk@outlook.com (W. Zuo).

https://doi.org/10.1016/j.aei.2026.104483
Received 25 August 2025; Received in revised form 8 December 2025; Accepted 13 February 2026

application of 3D printed TO designed joints in steel gridshell structures [26–28]. However, existing design standards, which predominantly rely on mechanical or semi-empirical formulations, are not suitable to address the intricate loading paths and numerous influencing factors associated with TO designed joints [29]. Furthermore, the inherently multi-objective nature of these designs—requiring a careful balance between the minimisation of material usage and mechanical robustness—presents additional challenges. The traditional manual iterative "forward design" approach (see Fig. 2), characterised by a theoretical model, design rules and manual iteration based on expert knowledge, struggles to optimise such conflicting objectives, underscoring the need for novel design methodology.

Surrogate-assisted multi-objective optimisation (MOO) has demonstrated success in domains such as building performance optimisation and engineering management [30–33]. For example, Liu et al. [34] proposed optimisation strategies for designing urban block forms considering daylight, energy consumption and photovoltaic energy potential, using parametric simulation tools and multi-objective algorithms within the Rhino-Grasshopper platform. Zhang et al. [31,35,36] have made significant advances using MOO in construction automation, structural health monitoring, and emergency response management. Similarly, Pan et al. [37] introduced a MOO framework for green building design, employing deep reinforcement learning to fine-tune design parameters. Although these advances represent significant strides in integrating artificial intelligence (AI) into architecture, utilizing AI to optimise structural performance remains relatively unexplored. Moreover, while data-driven machine learning (ML) and MOO can be implemented directly using general text programming platforms, solving architectural problems ultimately requires large commercial CAD software realising design schemes. However, conventional manual cross-platform transformations are inefficient, prone to data loss and lack real-time feedback, hindering interactive design and preventing seamless evaluation and optimisation of joint performance within design platforms.

This study seeks to address three key research challenges: (1) How to establish a rational performance evaluation system for TO design of steel gridshell joint, (2) How to establish a seamless transformation workflow integrating joint TO design, performance prediction and MOO, and (3) How to achieve a balance among weight, stiffness and stress uniformity for TO designed joints. To address these challenges, the present research leverages advances in ML, MOO, Clustering, parametric design, TO, subdivision surface modelling and reverse engineering, to offer two key contributions: (1) A seamless parametric design workflow: A novel integrated parametric workflow that tightly links TO, ML surrogate-based performance prediction, and MOO in a Rhino-Grasshopper environment was proposed for steel gridshell joints. This workflow enables automated generation and evaluation of optimised steel joint designs, providing real-time feedback and eliminating tedious cross-platform iterations, and (2) A multi-objective evaluation system and inverse design framework: A novel joint performance evaluation system that combines weight, stiffness and proposed stress uniformity considerations is proposed and integrated into a generative inverse design framework. This approach ensures optimal trade-offs between improving mechanical performance and material efficiency, providing a reasonable and practical basis for selecting optimal joint designs in steel gridshell structures.

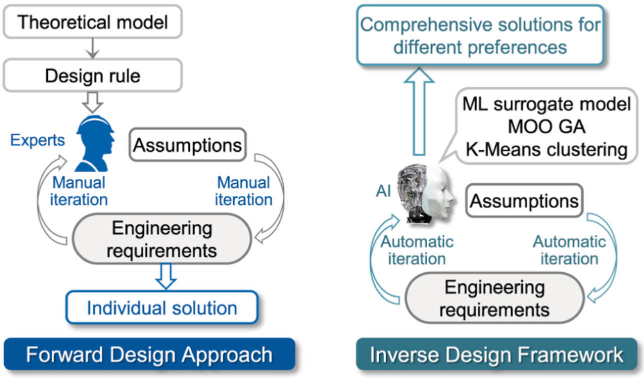

Fig. 2. Comparison of traditional "forward design" approach and proposed "inverse design" framework.

The remainder of this paper is structured as follows. Section 2 provides a comprehensive review of the progress and challenges in the TO design of gridshell joints. Section 3 describes the proposed framework and its constituent components. Section 4 validates the effectiveness of the framework through a case study of joints in steel gridshell structures. Section 5 discusses the broader implications of the method, particularly its potential for 3D printing applications. Finally, Section 6 concludes the study and outlines avenues for future research.

2. Literature review

The topology optimisation of steel joints in gridshell structure falls under the field of continuum topology optimisation [38]. Two of the most prominent methods in this domain are the Solid Isotropic Material with Penalization (SIMP) and the Evolutionary Structural Optimisation (ESO) approaches. The ESO method, which has evolved into the Bi-directional Evolutionary Structural Optimisation (BESO) approach [10,11,38], minimises compliance using element density as the design variable under volume constraints.

The advent of AM oriented TO design marks a new era in architectural and structural innovation [12–17,39–42]. Arup [43] applied the SIMP-based software to optimise critical joints in a large tensegrity structure, achieving significant weight reductions. Seifi et al. [44] utilised the BESO algorithm to optimise complex joints, including the Seele joint at London's Westfield Shopping Centre and the Sun Valley joint in

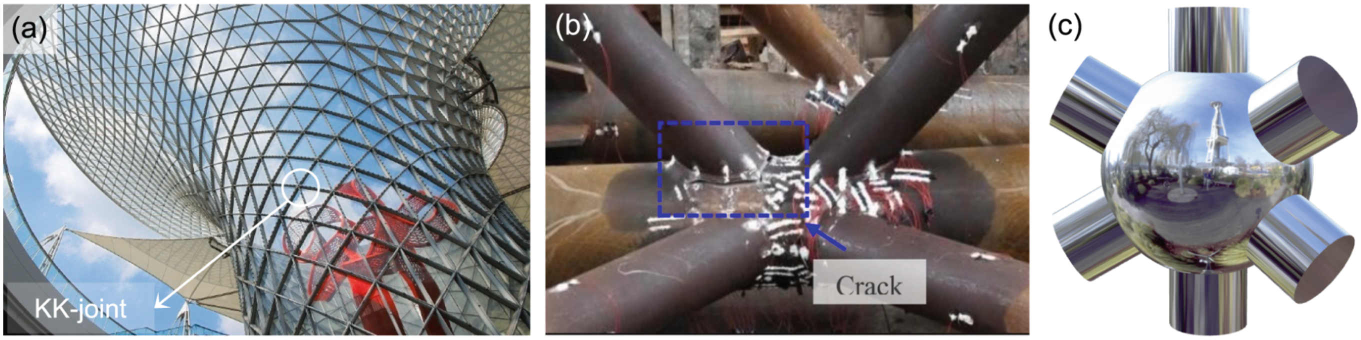

Fig. 1. Gridshell joints: (a) Sun Valley of the Shanghai Expo Axis; (b) KK-type joints with braces welded to a chord [4]; (c) joints with members welded to a hollow sphere.

the Shanghai Expo Axis. Laghi et al. [45] proposed an integrated design and fabrication framework that efficiently applies TO algorithms to enhance the efficiency of steel joints. This method was demonstrated through the re-design of joints in the British Museum gridshell roof structure. Despite these advances, Arup [43] had already identified limitations in the early stages, including the lack of interactivity and ease of operation. Additionally, these designs focused on isolated joint cases, underscoring the need to develop parameterised workflows for scaling this design methodology across all joints within a structure.

In the realm of metal 3D printing, Directed Energy Deposition (DED) and Powder Bed Fusion (PBF) are currently the most industrially applied technologies [29]. Among the DED processes, Wire Arc Additive Manufacturing (WAAM) stands out for its low equipment costs and the ability to produce large-scale components [46–52]. Moreover, WAAM-fabricated steels have demonstrated superior static and fatigue performance [53–57]. However, WAAM suffers from relatively low precision and the presence of surface undulations [58,59]. In contrast, Selective Laser Melting (SLM) [60–62], a PBF technology, offers superior precision, albeit with size limitations and higher costs; this technology is well suited for the fabrication of complex structures like TO designed joints in architecture.

Current research studies revealed that 3D-printed optimised steel joints possess superior structural performance compared to traditional joints. Kanyilmaz et al. [63,64] drew inspiration from the multi-chambered structure of bamboo to TO design tubular joints for a gridshell structure. They reduced peak stresses by approximately 70% and improved the ultimate load-bearing capacity by 2–3 times compared to traditional uniform hollow section joints. Deng et al. [65–67] further advanced the field by fabricating TO designed joints from carbon steel, high-strength and stainless steel using the SLM. Tests on these joints revealed significant differences in failure modes and load-bearing mechanisms between TO designed joints produced via advanced SLM techniques and those manufactured through conventional processes. These research highlights the uncertainties arising from numerous control parameters that influence the geometry and mechanical performance of TO designed joints. Conventional "forward design" approaches are unsuitable for TO designed joints. The lack of a robust methodology for evaluating mechanical performance limits the practical application of 3D-printed steel TO designed joints in engineering practice.

3. Methodology

3.1. Proposed parametric inverse design framework

The traditional "forward design" approach relies on labour-intensive adjustments, limiting exploration of the design space and often yielding suboptimal solutions due to human bias toward familiar configurations. It struggles to handle complex geometries or multi-objective trade-offs (e.g., weight versus structural performance), hindering data-driven optimisation and real-time feedback. This study proposes a generative inverse design framework (Fig. 2) for TO designed joints in steel gridshell. The "inverse design" framework is contrary to the above-mentioned conventional "forward design" approach. The AI-based inverse design framework can automatically obtain the optimal solution that achieves a balance among multiple design objectives, eliminating the need for manual iteration. Developed on the Rhino-Grasshopper parametric design platform, the proposed framework consists of three modules (see Fig. 3): Topology Optimisation Design (TOD), Surrogate Model Prediction (SMP) and Multi-objective Optimisation and Clustering (MOO-C), summarised as follows:

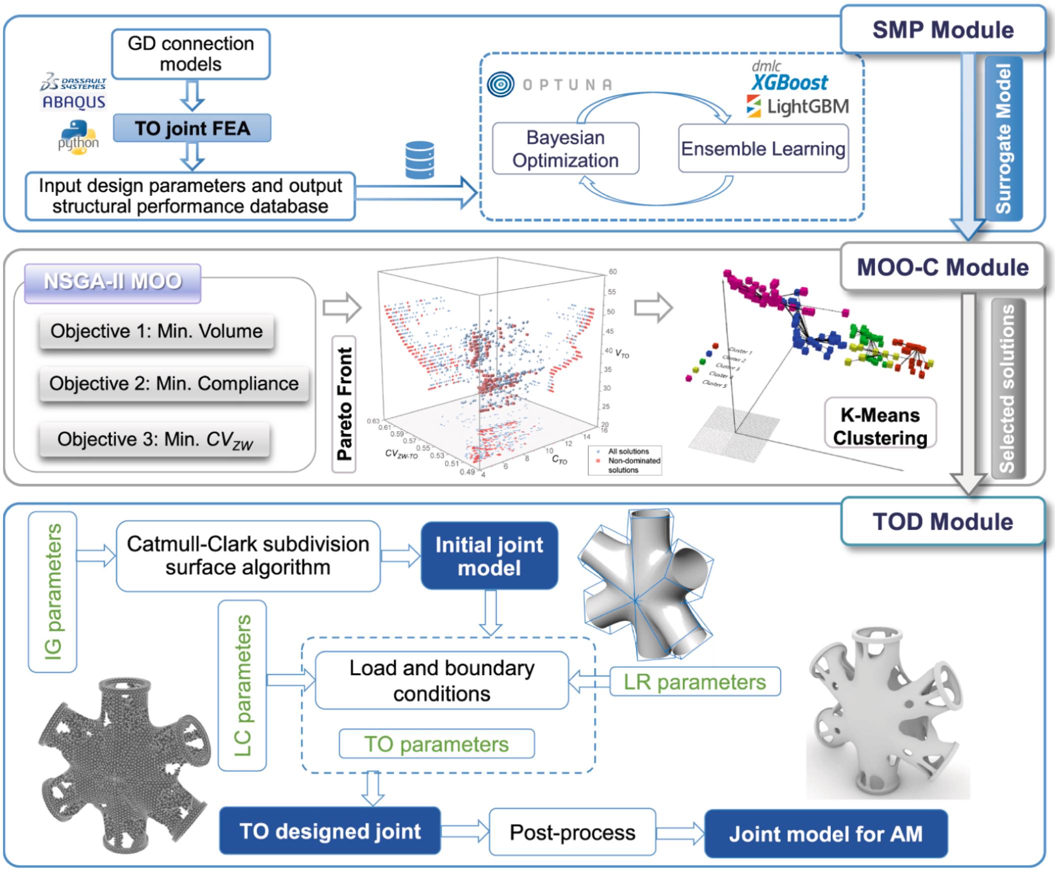

Fig. 3. Framework of generative inverse design platform.

- SMP Module: A Bayesian optimisation-based ensemble learning regressor is developed and trained to accurately predict the mechanical performance of TO designed joints. This high-precision regressor is integrated into the Grasshopper platform as a user-friendly parametric plugin, by combining Python scripting and the Grasshopper visual programming interface. This integration enhances efficiency in the subsequent MOO process by providing a reliable and accessible surrogate model for evaluating mechanical performance.
- MOO-C Module: The joint design problem is formulated as a multi-objective optimisation task in this module. The evaluation system of the MOO is guided by three core objectives: lightweight design, maximised stiffness and uniform stress distribution. It employs the NSGA-II algorithm to iteratively evaluate and refine design alternatives generated by the surrogate model. A Pareto-optimal solution set is identified to balance the competing objectives. These solutions are clustered into representative categories by the K-Means method to simplify the final joint selection.
- TOD Module: This module generates TO designed joint models based on the former selected input control parameters. The Catmull-Clark subdivision surface algorithm is adopted to generate smooth initial joint models. These models serve as the foundation for topology optimisation using the BESO algorithm. The TO design is executed on a cloud server decoupled from local computational threads. Once computing is complete, the results are retrieved and post-processed using advanced reverse engineering techniques. The designers could combine subjective preferences and design expertise to select the most suitable final design.

3.2. *Proposed joint performance evaluation system*

High-performance structural design aims to reduce weight for enhanced performance. While TO inherently prioritises lightweight objectives (material minimisation) and stiffness-based criteria, these two principles alone fail to address other challenges important for gridshell joints, particularly stress concentrations. However, the complex geometric features of TO-designed joints—such as thin-walled transitions, intricate branches, or abrupt curvature changes—can inadvertently introduce localised stress peaks, elevating fatigue failure risks for steel gridshell structures subjected to long-term cyclic loading. In this scenario, overstressed regions accelerate damage initiation, while underutilised low-stress zones result in material waste.

A third principle – stress uniformity – is therefore also considered, ensuring a uniform stress distribution serves dual purposes. First, it prevents premature fatigue failure by controlling high-level stresses below critical thresholds, ensuring joints do not fail before connected members. Second, it optimises material utilization by eliminating inefficient material in low-stress areas and redistributing mass to high-stress zones. Unlike stiffness or weight metrics, stress uniformity directly bridges geometric design, mechanical behaviour and lifecycle performance, making it indispensable for balancing competing priorities in gridshell TO joints. Thus, the proposed joint performance evaluation system—integrating weight, stiffness and stress uniformity—enables a holistic evaluation, ensuring joints achieve not only efficiency and safety but also manufacturability and long-term resilience. The following multi-objective optimisation system is proposed:

$$\begin{cases} \text{Minimise: } F(X) = \{f_1(X), f_2(X), f_3(X)\} \\ \text{Subject to: } X \in D_{LP} \cup D_{TOP} \\ \qquad\qquad\quad X = (x_1, x_2, \ldots x_k)^T \end{cases} \tag{1}$$

where $f_1(X), f_2(X), f_3(X)$ represent 3 sets of objective functions mentioned above, and X is a feature vector composed of k variables x_i from a feasible space. The feasible space is the union of loading range parameters (D_{LP}) and topology optimisation parameters (D_{TOP}) in the "four-dimensional" variables.

The first objective function addresses the lightweight design by minimising the material volume of a TO designed joint (V_{TO}):

$$\text{Min. } f_1(X) = V_{TO} \tag{2}$$

Joint stiffness is a critical mechanical metric affecting overall gridshell structural dynamics, stability and load-bearing capacity. Maximising the stiffness of TO designed joints corresponds to minimising the compliance C_{TO}, which is calculated via FEA as the strain energy (i.e., the energy stored due to the structural deformation) and is adopted as the second objective:

$$\text{Min. } f_2(X) = C_{TO} \tag{3}$$

The ideal joint is expected to have evenly distributed stress across the joint. The coefficient of variation (CV) of the von Mises stresses over the joint volume can be used to evaluate the uniformity of the stress distribution:

$$CV = \frac{\sigma_{std}}{\mu} \tag{4}$$

in which,

$$\mu = \frac{1}{N}\sum\nolimits_{i=1}^{N} f_i \tag{5}$$

and

$$\sigma_{std} = \sqrt{\frac{1}{N}\sum\nolimits_{i=1}^{N} (f_i - \mu)^2} \tag{6}$$

where N is the total number of finite elements, $\boldsymbol{f_i}$ is the stress value of the i th element, $\boldsymbol{\mu}$ is the average stress value of all elements, and $\boldsymbol{\sigma_{std}}$ is the standard deviation of the stress. The dimensionless metric CV measures relative dispersion, enabling comparisons of material utilization efficiency across different materials or designs. However, for complex structures with many elements, the traditional CV metric is insufficiently sensitive to a small number of high-risk elements with stresses near or exceeding the yield strength (stress hotspots) or underutilised elements with excessively low stresses.

Algorithm 1. (*Calculation of Zonal Weighted Coefficient of Variation* (CV_{ZW}))

```
Require: $f_y$: Yield strength, $S$: List of stress values, $W$: Weights $\{w_{low}, w_{med}, w_{high}\}$
Ensure: $CV_{ZW}$: Corrected Coefficient of Variation

$T_{low} \leftarrow 0.25 f_y,\ T_{high} \leftarrow 0.75\, f_y$
$Z \leftarrow \{low: [],\ med: [],\ high: []\}$
for each $f$ in $S$ do
    if $f \le T_{low}$ then $Z[low].append(f)$
    else if $f > T_{high}$ then $Z[high].append(f)$
    else $Z[med].append(f)$
    end if
end for
$\mu \leftarrow \frac{1}{\mathrm{len}(S)}\sum\nolimits_{i=1}^{\mathrm{len}(S)} f_i$
for each zone in $Z$ do
    if $Z[zone] \ne []$ then
        $\sigma[zone] \leftarrow \sqrt{\frac{1}{\mathrm{len}(Z[\mathrm{zone}]) - 1}\sum\nolimits_{i \in Z[\mathrm{zone}]} (f_i - \mu)^2}$
    end if
end for
$N \leftarrow n_{low} + n_{med} + n_{high}$
$CV_{contrib} \leftarrow 0$
for each zone in $Z$ do
    $n_{zone} \leftarrow len(Z[zone])$
    if $\sigma[zone] > 0$ then
        $CV_{contrib} \leftarrow CV_{contrib} + \left(\frac{\sigma[\mathrm{zone}]}{\mu}\right)^2 \times \frac{n_{\mathrm{zone}}}{N} \times W[zone]$
    end if
end for
$CV_{ZW} \leftarrow \sqrt{CV_{contrib}}$
return $CV_{ZW}$
```

A novel von Mises stress evaluation metric is therefore proposed, improving upon the traditional coefficient of variation (CV)-based method by introducing a Zonal Weighted coefficient of variation (CV_{ZW}) metric (as demonstrated in Algorithm 1). The CV_{ZW} metric divides element stress values (S) into three zones (Z), i.e., low, medium and high stress zones, assigning different weights (W) to each zone. This approach allows a more comprehensive and targeted assessment of the stress distribution variability. By incorporating material strength characteristics, the weighted coefficient of variation better captures the stress distribution heterogeneity across different stress zones, providing a more accurate measure of potential stress concentrations and their impact on the fatigue performance of the TO designed joints. The third objective function is:

$$\text{Min. } f_3(X) = CV_{ZW} \tag{7}$$

3.3. SMP Module

A seamless interaction between the Grasshopper 3D design platform and the external VS Code text programming environment was established in the SMP Module. Within the Python framework in VS Code, a Bayesian optimisation-based ensemble learning regressor was developed and trained to accurately predict the mechanical performance of TO designed joints. The trained regressor was seamlessly integrated into the Grasshopper platform as a user-friendly parametric add-on. This integration enhances efficiency in the subsequent MOO process by providing a reliable and accessible surrogate model for evaluating mechanical performance of the TO designed joints.

A pre-processed dataset in.csv format was divided into training and testing subsets in an 8:2 ratio. The input parameters of the TOSG plugin were controlled by a “four-dimensional” design variable system, ensuring comprehensive and flexible control over the modelling and optimisation process. These dimensions include initial geometric (IG) parameters, loading condition (LC) parameters, loading range (LR) parameters and topology optimisation (TO) parameters. The IG parameters include member dimensions and positional relationships, which were used to generate various initial nodal models for analysis. The LC parameters define variables such as load magnitudes and application directions, considering diverse geometric conditions during the topology optimisation phase of the joint design. The LR parameters specify the loading regions and forms, providing precise control over the areas subjected to mechanical forces and their distributions. The TO parameters cover variables related to the TO algorithm, such as target volume fractions, filter radii and other critical settings that influence the optimisation results. The output parameters represent the mechanical performance indices of the TO designed joints. Feature standardization (via the Z-Score method) and target transformation (via the Yeo-Johnson method) were applied to normalise the dataset. The Z-score method removes scale imbalance and improves optimiser stability; the Yeo-Johnson method reduces right-skew and variance heterogeneity, providing robustness for present and future datasets.

The XGBoost [68] ensemble learning regression model was trained separately for each target variable. Hyperparameter optimisation was conducted using the Tree-structured Parzen Estimator (TPE) Bayesian optimisation (BO) algorithm [37,69], minimising negative mean squared error as the objective function. Unlike grid or random search approaches, which rely on exhaustive or random sampling, BO constructs a surrogate probabilistic model to approximate the objective function. The key hyperparameters, including the number of trees, maximum depth, learning rate, and regularization terms (L_1 and L_2), were tuned over a given number of iterations. To enhance efficiency, a median stopping method halted suboptimal trials early. Model performance was evaluated through K-fold cross-validation, which aggregated results from multiple training-validation splits to provide a robust performance assessment. The metrics Root Mean Squared Error (*RMSE*), Mean Absolute Error (*MAE*), Coefficient of Determination (R^2) and Mean Absolute Percentage Error (*MAPE*), were used to evaluate the surrogate model robustness. The pre-processing feature and target transformers, alongside the trained models, were saved in.pkl format for future use.

Building upon this optimised model, a custom parametric design add-on, *TOSG*, was developed on the Rhino-Grasshopper platform using *GH_CPython* within an Anaconda Python 3.11 environment. The *TOSG* add-on provides an intuitive interface for predicting the performance of the TO designed joints through simple input–output configurations. This streamlined parameter configuration allows users to interface directly with pre-trained machine learning models. The custom plugin operation workflow is illustrated in Fig. 4, featuring the following input and output parameters:

- Input Parameters (Left Side):

path: A string input specifying the file path to the ensemble learning model.

x: One-dimensional feature vector denoting unstandardised feature data.

algo: A string input defining the machine learning algorithm type to be used.

- Output Parameters (Right Side):

label 1 ~ n: The predicted mechanical performance metrics 1 ~ n.

3.4. MOO-C Module

Traditional MOO is computationally expensive and time-consuming, since it generates large numbers of digital models in each generation of population evolution and performs finite element analysis (FEA) to obtain the objective performance parameters. To address these challenges, a custom parametric MOO with surrogate models was implemented as shown in Fig. 4. By leveraging ML models as a surrogate for finite element analysis (FEA), the proposed method eliminated the need for generating finite element models and significantly reduced computational costs. The framework integrated Python scripting within a visual programming environment, enabling the rapid evaluation of objective parameters and facilitating efficient optimisation convergence. The MOO problem was solved by Non-dominated Sorting Genetic Algorithm II (NSGA-II) [70], whose elitist non-dominated sorting and crowding-distance diversity preservation yielded well-spread Pareto sets for non-convex, three-objective optimisation at modest computational cost.

Step 1: Population initialization. Two dimensional design variables featuring the IG and LC parameters were derived through parametric structural modelling and directly input into the optimiser as fixed parameters. An initial virtual population P_0 of size N was randomly generated, using the remaining two dimensional design variables, namely, the LR and TO parameters. Each individual $\boldsymbol{X_i}$ in P_0 was associated with three objectives: volume $f_1(X_i)$ derived using Grasshopper's surface analysis tool and calculated through volumetric evaluation, compliance $f_2(X_i)$ and CV_{ZW} coefficient $f_3(X_i)$ predicted by the surrogate model with the aid of the custom *TOSG* add-on.

Step 2: Fast non-dominated sorting. The population was sorted into Pareto fronts F_1, F_2, F_3 based on dominance criteria. An individual X_1 is considered to dominate another individual X_2 if the following conditions are satisfied:

$$\forall j \in \{1,2,3\}, f_j(X_1) \le f_j(X_2), \text{ and } \exists k \in \{1,2,3\}, f_k(X_1) \le f_k(X_2) \tag{8}$$

To ensure diversity among solutions on the same front, the crowding distance d_i was calculated as:

$$d_i = \sum_{j=1}^{3} \frac{f_j(X_{i+1}) - f_j(X_{i-1})}{f_j^{max} - f_j^{min}} \tag{9}$$

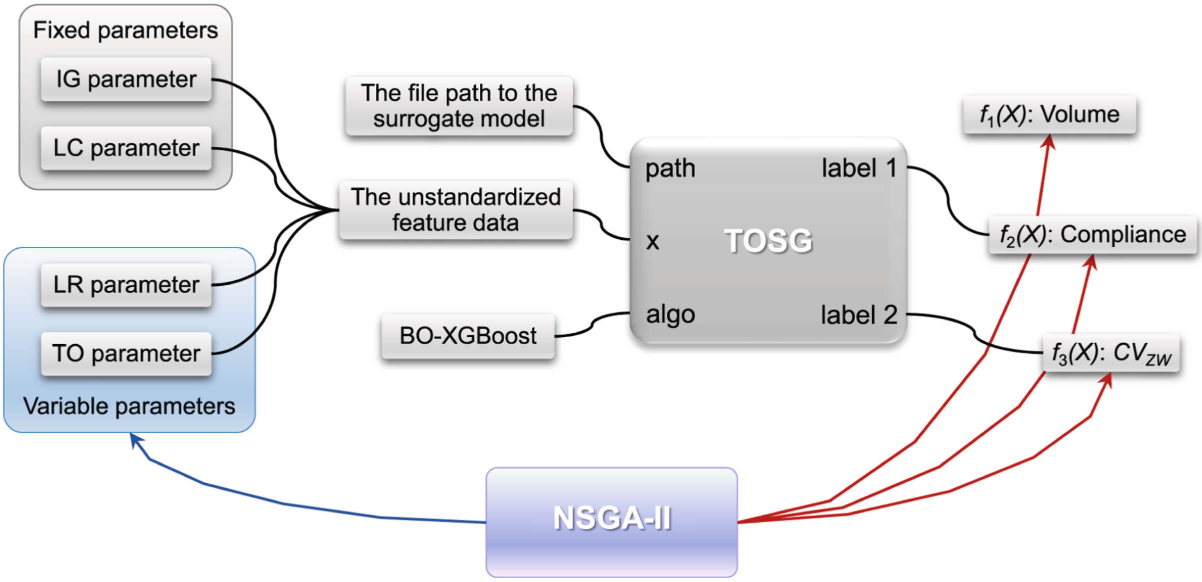

Fig. 4. Parametric procedure of surrogate model based MOO.

where $f_j(X_{i+1})$ and $f_j(X_{i-1})$ are the objective values of the neighbouring individuals in the j th objective dimension, f_j^{max} and f_j^{min} represent the maximum and minimum values for that objective in the current front.

Step 3: Offspring generation. The selection process used tournament selection, prioritizing solutions with better Pareto ranks and higher crowding distances, to select parent individuals. Simulated binary crossover (SBX) and polynomial mutation (PM) were applied to generate offspring with diverse characteristics.

Step 4: Population update. The combined population $R_t(= P_t \cup Q_t)$ was sorted, and the next generation P_{t+1} was selected based on Pareto dominance and crowding distance until termination criteria, such as a maximum number of iterations T_{max}, were met. If the termination criteria were satisfied, the algorithm outputs the Pareto-optimal front, representing the non-dominated solutions achieving trade-offs among the multiple objective functions.

The TO designed joint solutions set on the Pareto front were large and complex, making it challenging to use directly for final selection. By applying K-Means Clustering analysis, these solutions were grouped into several representative clusters, where the solutions within each cluster share similar characteristics. This approach reduced the number of solutions to be considered, streamlining the decision process. The clustering began by randomly selecting k optimised joint solutions points as the initial cluster centres. Each point was then assigned to the cluster whose centre is closest, based on a distance metric such as the Euclidean distance, calculated as $\text{argmin}_k \|x_i - \mu_k\|^2$, where x_i represents the data point, μ_k is the centre of cluster k, and $\|x_i - \mu_k\|^2$ is the squared Euclidean distance. Once all points were assigned, the cluster centres were recalculated by computing the mean of all data points within each cluster, expressed as:

$$\mu_k = \frac{1}{|C_k|}\sum\nolimits_{x_i \in C_k} x_i \tag{10}$$

where C_k is the set of data points in cluster k, and $|C_k|$ is the number of points in the cluster. This process of assigning points to the nearest cluster and updating cluster centres was repeated iteratively until the cluster centres converged or a predefined number of iterations were reached, resulting in well-separated and meaningful TO designed joints clusters.

3.5. *TOD Module*

This module employed an integrated parametric workflow developed for TO design of steel joints in gridshell structures based on the Rhino-Grasshopper platform, as illustrated in Fig. 3. Based on the joint IG parameters derived from the architectural scheme of the gridshell, the Catmull-Clark subdivision surface algorithm was employed to generate smooth initial joint models. These pre-designed models served as the foundation for topology optimisation using the BESO algorithm. The LC parameters were typical load combinations derived from the gridshell structural analysis. The LR and TO parameters were dependent on the MOO results. Once optimisation was complete, the results were post-processed using advanced reverse engineering techniques to achieve smooth and closed solid joint models.

The Catmull-Clark subdivision surface technique [71] was employed to generate smooth initial joint geometry from a coarse control mesh to eliminate sharp corners and reduce stress concentrations before topology optimisation. All joint IG dimensional control parameters, together with their corresponding coordinates, were extracted from a parametric architectural model based on the Rhino-Grasshopper platform. The extracted parameters were fed into a custom component to generate an initial subdivision control mesh, designed to align with the geometric characteristics of gridshell joints. Using the Catmull-Clark subdivision surface algorithm, the control mesh underwent iterative refinement, producing a series of higher-resolution subdivision meshes. The resulting subdivision surfaces were refined into watertight models using automated capping techniques, providing closed geometries ready for topology optimisation.

A parametric TO design and post-processing program of steel joints in gridshell was developed using a combination of text-based scripting and visual programming. The joint TO design was conducted using BESO based on the subdivision surface joint models developed in the initial phase. The BESO algorithm is a robust and widely used method developed by Xie's Group [10,11,38] for topology optimisation. It iteratively optimises the distribution of material within a defined design domain to achieve a balance between structural performance and material efficiency. The finite element mesh of the initial joint model was generated based on a sensitivity analysis to determine an optimal mesh density that achieved a balance between computing time and accuracy. The loads and boundary conditions for the joints were derived from typical load cases and boundary combinations from parametric structural analysis. Key parameters, such as the target volume fraction, which represents the ratio of the target material volume to the total design domain volume, as well as the evolutionary rate, filter radius and maximum iteration limits, were input into the solver. The optimisation process was executed on a cloud server, enabling efficient computations that were decoupled from local resources.

Transitioning from TO models to manufacturable geometries necessitates a multi-stage reverse engineering pipeline to mitigate inherent defects: non-manifold edges, surface discontinuities, and irregular tessellations. The fractured TO mesh is converted into a sparse hierarchical signed distance field (SDF) using OpenVDB [72]. The resulting manifold mesh, while topologically sound, exhibits grid-aligned surface noise from voxelization. Laplacian smoothing is applied to attenuate these high-frequency irregularities while preserving the underlying macroscopic form. QuadriFlow [73] is employed, utilizing a globally guided orientation field to produce a scalable, coherent quad layout that preserves sharp features and curvature-driven edge alignment. Catmull-Clark subdivision surfaces are then applied to iteratively refine the quad mesh. Prior to fabrication, the final model undergoes rigorous validation for watertightness and printability, ensuring compliance with manufacturing constraints (minimal wall thickness, self-supporting angle tolerances). Validated models are imported into *Rhino*, converted into NURBS surfaces for CAD compatibility, and exported as.stp files for numerical analysis or.stl files for 3D printing, ensuring readiness for downstream applications.

4. Case study

4.1. General

To assess the capability of the developed generative inverse design framework, six-member tubular gridshell joint is employed as the representative case study. The gridshell joint is generated by the following four dimensional parameters:

- IG Parameters: $d_{T,0}$ denotes the diameter of the chord, $d_{T,1}/d_{T,0}$ denotes the ratio of the brace diameter to the chord diameter, θ_i denotes the in-plane angle between the brace and the chord and θ_o denotes the out-of-plane angle between the brace and the chord. The IG Parameters controlled subdivision surface of a typical six member-type joint is shown in Fig. 5(a).
- LC Parameters: L denotes the axial force applied to the joint ends, φ denotes the angle of application for the equivalent bending moments and ML denotes the magnitude of the equivalent bending moment. The LC Parameters controlled joint loading scheme is shown in Fig. 5 (b).
- LR Parameters: The equivalent bending moment was applied uniformly to each member along the subdivision surface edges. $X_0/d_{T,0}$ denotes the ratio of the chord equivalent bending moment loading domain width to the chord diameter, $Y_0/d_{T,0}$ denotes the ratio of the chord loading domain height to the chord diameter, $X_1/d_{T,1}$ denotes the ratio of the brace loading domain width to the brace diameter and $Y_1/d_{T,1}$ denotes the ratio of the brace loading domain height to the brace diameter.
- TO Parameters: d_{mean}/S_m denotes the ratio of the mean member diameter to the minimum TO finite element mesh size, TV denotes the ratio of the target volume to the initial design domain volume and R_{min}/S_m denotes the ratio of the filter radius to the minimum TO mesh size.

The structural performance of the optimised joints was analysed using the FEA software *ABAQUS*. The material properties of SLM 316 L stainless steel reported in [17,40] were adopted. The nodal degrees of freedom at the end section of each connecting member were kinematically coupled to an assigned reference point, which was used to impose boundary conditions and apply the prescribed loading. Pinned boundary constraints were applied to the chords ends, where one end was only permitted to rotate while the other end was permitted to rotate and translate along the local longitudinal axis direction (Fig. 5(b)). The topology optimised joint models were meshed using the three dimensional second-order interpolation tetrahedral element of C3D10 in this study. Mesh convergence analysis was performed to achieve a balance between the accuracy and computational efficiency [74,75].

4.2. Establishment of database

A comprehensive database that linked the four-dimensional control parameters of the gridshell TO designed joints with their corresponding mechanical performance characteristics was created, facilitating the development of the machine learning models. The database establishment procedure is illustrated in Fig. 6. All design features were continuous variables, and the range of parameter values was determined not only by adhering to the fundamental requirements of the CIDECT standards [76] but also by ensuring the overall rationality of multi-parameter combinations across various scales. Table 1 presents the specific control parameters and their corresponding ranges for the generation of TO designed joints in gridshell structures. To reduce the number of required training samples while maintaining their representativeness, Latin Hypercube Sampling (LHS) was employed for random sampling of the TO designed joints control parameters within the high-dimensional design space. The LHS method divides the range of each parameter into equal intervals, and a sample point is randomly selected from each interval [31,36]. This ensures that each parameter dimension is uniformly covered, with every interval sampled at least once.

A total of 8,963 valid parameter sets were generated using this

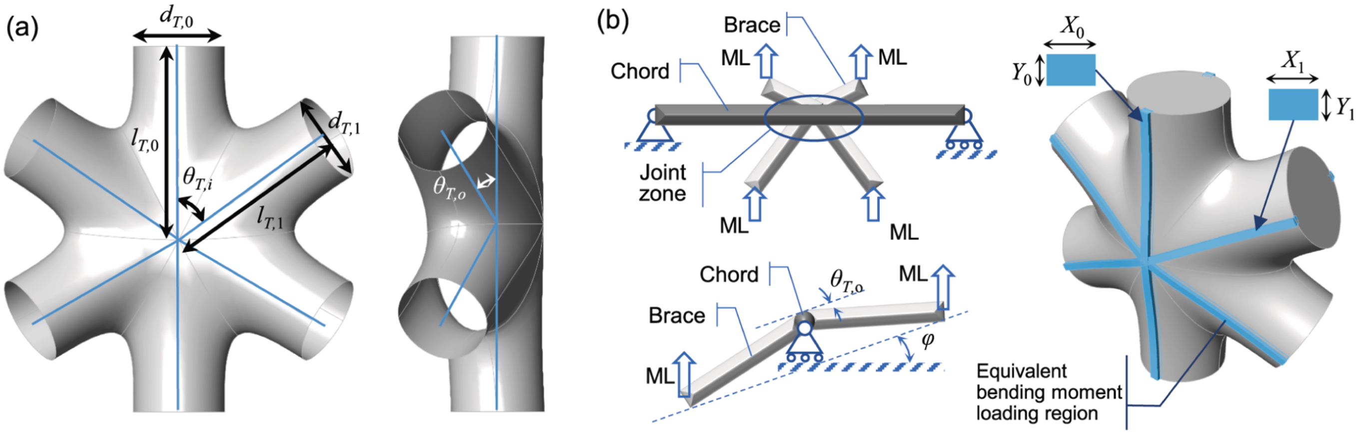

Fig. 5. Definition of parameters: (a) IG parameters controlled subdivision surface of six member-type joint; (b) LC parameters controlled joint loading scheme.

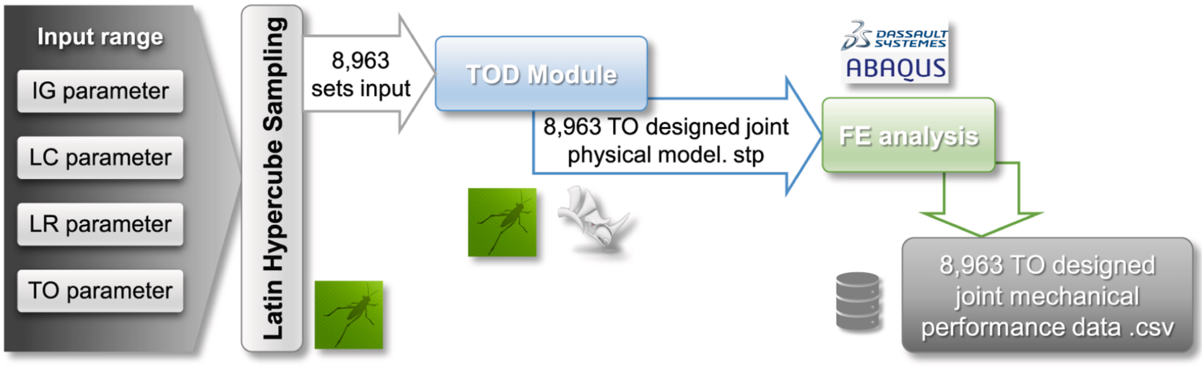

Fig. 6. Database establishment procedure.

Table 1
Control parameters and ranges for generation of TO designed joints.

Dimension	Parameter	Range	Unit
IG Parameter	$d_{T,0}$	[100,250]	mm
	$d_{T,1}/d_{T,0}$	[0.6, 1.2]	–
	θ_i	[50,65]	°
	θ_o	[5,25]	°
LC Parameter	L	[-30, 30]	kN
	Φ	[0,180]	°
	ML	[0, 30]	kN
LR Parameter	$d_{T,0}/X_0$	[20,30]	–
	$d_{T,0}/Y_0$	[20,30]	
	$d_{T,1}/X_1$	[20,30]	
	$d_{T,1}/Y_1$	[20,30]	
TO Parameter	d_{mean}/S_m	[15,25]	–
	R_{min}/S_m	[1,3]	
	TV	[0.25, 0.5]	

approach. These parameter sets were sequentially input into the TOD Module to generate TO designed joint geometric models. The computational process was distributed across multiple cloud servers. The resulting.stp files for each TO designed joint geometric model were imported into ABAQUS using a customed parametric automated CAE workflow to simulate the structural behaviour. The finite element simulations were performed on several local high-performance workstations in parallel. The FEA outputs of mechanical performance data for each TO designed joint were collected and organised. The input and output data were subsequently exported in.csv format, creating a relational database.

4.3. Parametric BO-XGBoost surrogate model establishment

To enhance the predictive performance of the XGBoost model for the two target metrics, C_{TO} and $CV_{ZW\text{-}TO}$, the Bayesian Optimisation algorithm was employed to explore the hyper-parameter space to identify optimal configurations that minimise prediction error. The hyper-parameter optimisation process is shown in Fig. 7 using parallel coordinate plots, where the objective metric represents the mean negative MSE of the K-fold cross-validated predictions. The optimal hyper-parameter settings for the two prediction objectives are summarised in Table 2. These optimised parameters significantly enhanced the predictive accuracy of the model for both C_{TO} and $CV_{ZW\text{-}TO}$, demonstrating the effectiveness of BO in hyper-parameter tuning for high-dimensional regression tasks.

The trained BO-XGBoost model was integrated into a custom add-on of *TOSG*, as illustrated in Fig. 8. In this workflow, four-dimensional parameters were converted into a one-dimensional feature vector and then input into the *TOSG* add-on on the left side. The *TOSG* add-on automatically performed several operations: first, it normalised the features using a preconfigured Z-score transformer; next, it invoked the trained BO-XGBoost model to obtain predictive results; finally, it applied an inverse Yeo-Johnson transformation to output the two target mechanical performance indicators, C_{TO} and $CV_{ZW\text{-}TO}$, on the right side. By leveraging this parametric machine learning surrogate model, the subsequent MOO no longer required generating actual geometric models or performing FEA, thus avoiding the extensive computational resources typically consumed during such iterative procedures.

4.4. MOO

The surrogate-based multi-objective optimisation was automatically conducted on the Rhino-Grasshopper platform. The NSGA-II algorithm was employed, with a population size of 35 individuals per generation over 70 generations, resulting in the evaluation of 2450 virtual TO designed joints. The total design parameter space comprised 6.2×10^{11} configurations. The crossover and mutation probabilities were set at 0.9 and 1/3, respectively, with distribution indices fixed at 20. To evaluate optimisation effectiveness, 200 TO designed joints were randomly generated using LHS without MOO, and their predicted mechanical performance was compared against non-dominated solutions. The mechanical performance of both the MOO and randomly generated TO designed joints were obtained via surrogate models.

To assess the convergence and variability of fitness values across generations, standard deviation curves of the three objectives (V_{TO}, C_{TO} and $CV_{ZW\text{-}TO}$) were examined, examples of which are plotted in Fig. 9. All objectives show rapid improvement within the first 15 generations followed by stabilisation. Compliance (C_{TO}) exhibits the most pronounced drop in mean value. Its standard deviation exhibits a brief initial rise, followed by a gradual reduction and stabilisation as the search moves into exploitation and convergence. The mean value of the stress uniformity factor ($CV_{ZW\text{-}TO}$) reduces steadily. The standard deviation of $CV_{ZW\text{-}TO}$ collapses quickly in the early generations and remains low, indicating consistent responses among surviving designs. The mean value of volume (V_{TO}) decreases modestly at the outset and then oscillates around a plateau. Its standard deviation remains relatively steady, which reflects the algorithm maintaining diversity in material-use solutions along the Pareto front. In general, compliance optimisation exhibits the most significant reduction, with mean C_{TO} values decreased by 30%–37%. V_{TO} and $CV_{ZW\text{-}TO}$ experience mean reductions of approximately 10% and 7%, respectively. These results demonstrated the effectiveness of the optimisation process, with all objectives achieving improvements and stabilizing in the mid-to-late iterations. However, due to dimensional disparities among objectives, further analysis of fitness rankings and Pareto front distributions is essential for a comprehensive evaluation.

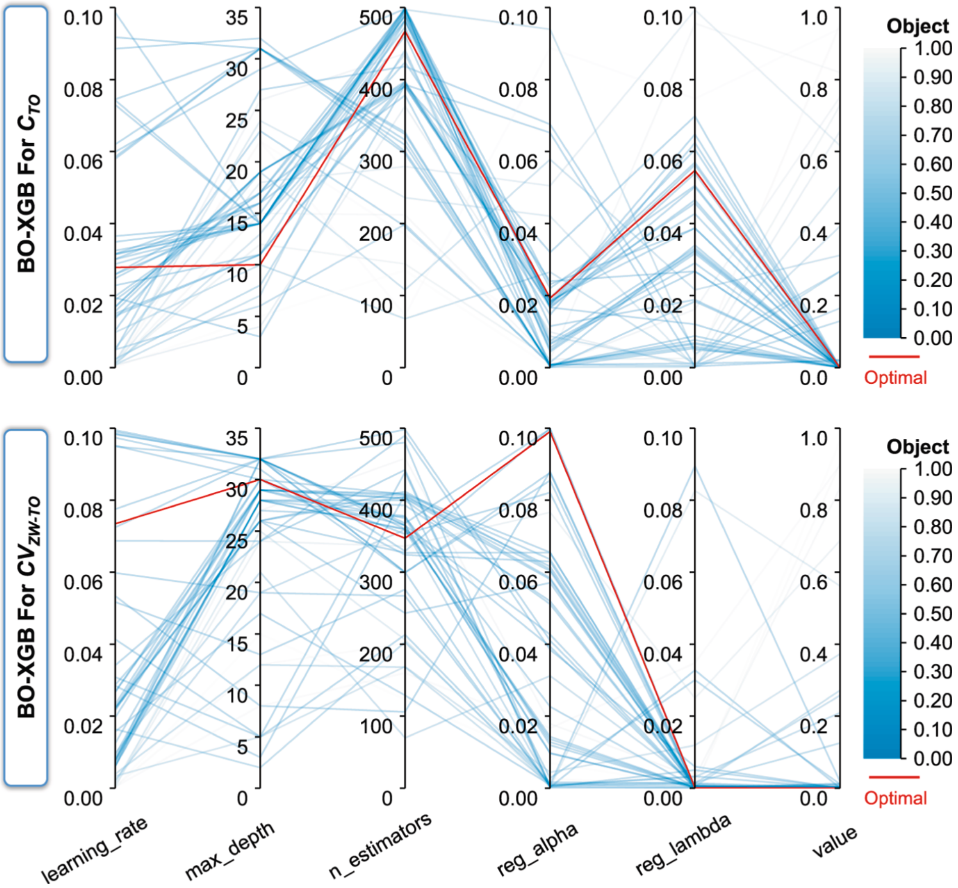

Fig. 7. BO-XGBoost hyper-parameter optimisation process.

Table 2
Summary of the best hyper-parameters.

Hyper-parameter	Meaning	Range	Value for C_{TO}	Value for $CV_{ZW\text{-}TO}$
n_estimators	number of trees	[]	467	347
max_depth	maximum depth	[2,32]	10	30
learning_rate	learning rate	[1e-4, 1e-1]	0.0279	0.0734
reg_alpha	L_1 regularization terms	[1e-4, 1e-1]	0.0193	0.0990
reg_lambda	L_2 regularization terms	[1e-4, 1e-1]	0.0548	0.0001

Among the 2450 feasible solutions, 196 non-dominated solutions were identified and mapped in space (Fig. 10). The objectives C_{TO}, $CV_{ZW\text{-}TO}$ and V_{TO} are plotted on the X, Y, and Z axes, respectively. Blue-grey spheres represent all feasible solutions, while red cubes denote the non-dominated solutions. Their projections onto the XY, YZ and XZ planes are illustrated as blue and red points, respectively. The non-dominated solutions are concentrated near the origin, forming a distinct Pareto front that highlights their superior performance compared to other feasible solutions. The Pareto front spans a broad range, demonstrating notable diversity. The ranges for the three objectives within the non-dominated set are $V_{TO} = 25.1 \times 10^{-3}$ m^3 to 50.8×10^{-3} m^3, $C_{TO} = 4.51$ Nm to 12.33 Nm, $CV_{ZW\text{-}TO} = 0.501$ to 0.552. These ranges encompass the minimum feasible values of the entire solution set while including the majority of optimal feasible solutions. The distribution of the Pareto front highlights significant diversity and comprehensive coverage, providing a robust basis for selecting optimised designs. However, selecting a final design from the non-dominated set remains challenging and necessitates additional criteria to balance competing objectives effectively.

To analyse all non-dominated solutions obtained from the MOO, the K-means Clustering method was applied. The optimal number of clusters was determined to be five, and the results are visualised in Fig. 11. Clusters, denoted as C1 to C5, are distinguished by different colours, demonstrating strong cohesion within clusters and high separability between them. The clustering process effectively grouped the non-dominated solutions into distinct categories, facilitating further analysis of design parameters and objective performances.

5. Discussion

5.1. Surrogate model validation

The performance of the BO-XGBoost surrogate model is summarised in Table 3. All evaluations were conducted by comparing the predicted values (transformed back using the inverse Yeo-Johnson transformation) against the actual original data. The comparisons between actual and predicted metrics are visualised in Fig. 12, where $C_{TO,\ A}$ and $C_{TO,\ P}$ represent the actual and predicted C_{TO} values and $CV_{ZW\text{-}TO,\ A}$ and $CV_{ZW\text{-}TO,\ P}$ represent the actual and predicted $CV_{ZW\text{-}TO}$ values.

As shown in Table 3, the R^2 values for both the training and testing datasets are consistently close to unity, indicating an excellent fit and robust explanatory power. The *MAPE* for both objectives are below 3%, consistent with the high prediction accuracy levels reported in existing structural performance machine learning studies [77–79]. Fig. 12(a) and (c) depict the relative frequency histograms of the ratio between the actual and predicted values for C_{TO} and $CV_{ZW\text{-}TO}$, respectively. The error distributions are consistent between the training and testing datasets, suggesting no signs of overfitting. Furthermore, the metrics *RMSE* and *MAE* in Table 3 confirm minimal discrepancies between the predicted

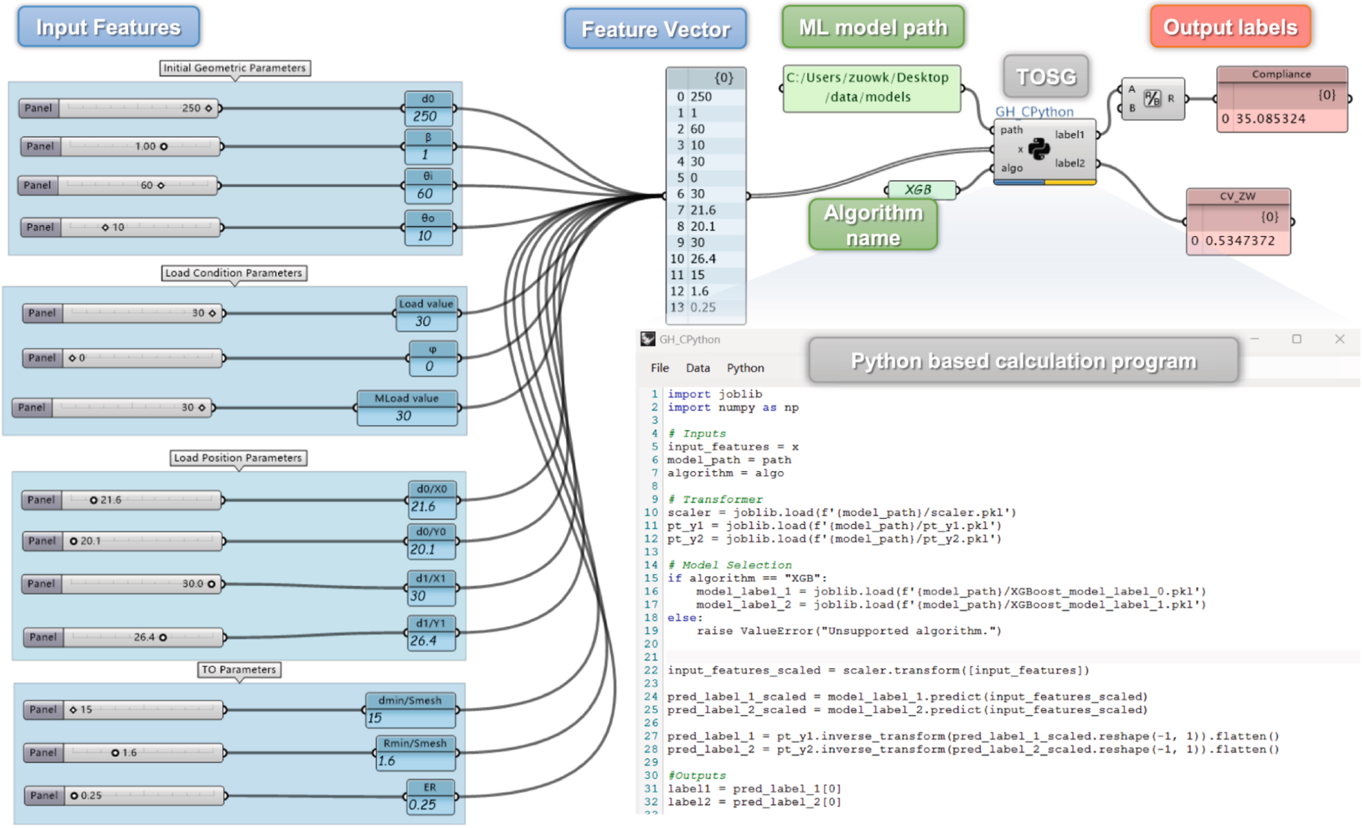

```python
import joblib
import numpy as np

# Inputs
input_features = x
model_path = path
algorithm = algo

# Transformer
scaler = joblib.load(f'{model_path}/scaler.pkl')
pt_y1 = joblib.load(f'{model_path}/pt_y1.pkl')
pt_y2 = joblib.load(f'{model_path}/pt_y2.pkl')

# Model Selection
if algorithm == "XGB":
    model_label_1 = joblib.load(f'{model_path}/XGBoost_model_label_0.pkl')
    model_label_2 = joblib.load(f'{model_path}/XGBoost_model_label_1.pkl')
else:
    raise ValueError("Unsupported algorithm.")


input_features_scaled = scaler.transform([input_features])

pred_label_1_scaled = model_label_1.predict(input_features_scaled)
pred_label_2_scaled = model_label_2.predict(input_features_scaled)

pred_label_1 = pt_y1.inverse_transform(pred_label_1_scaled.reshape(-1, 1)).flatten()
pred_label_2 = pt_y2.inverse_transform(pred_label_2_scaled.reshape(-1, 1)).flatten()

#Outputs
label1 = pred_label_1[0]
label2 = pred_label_2[0]
```

Fig. 8. Custom parametric machine learning model add-on of *TOSG*.

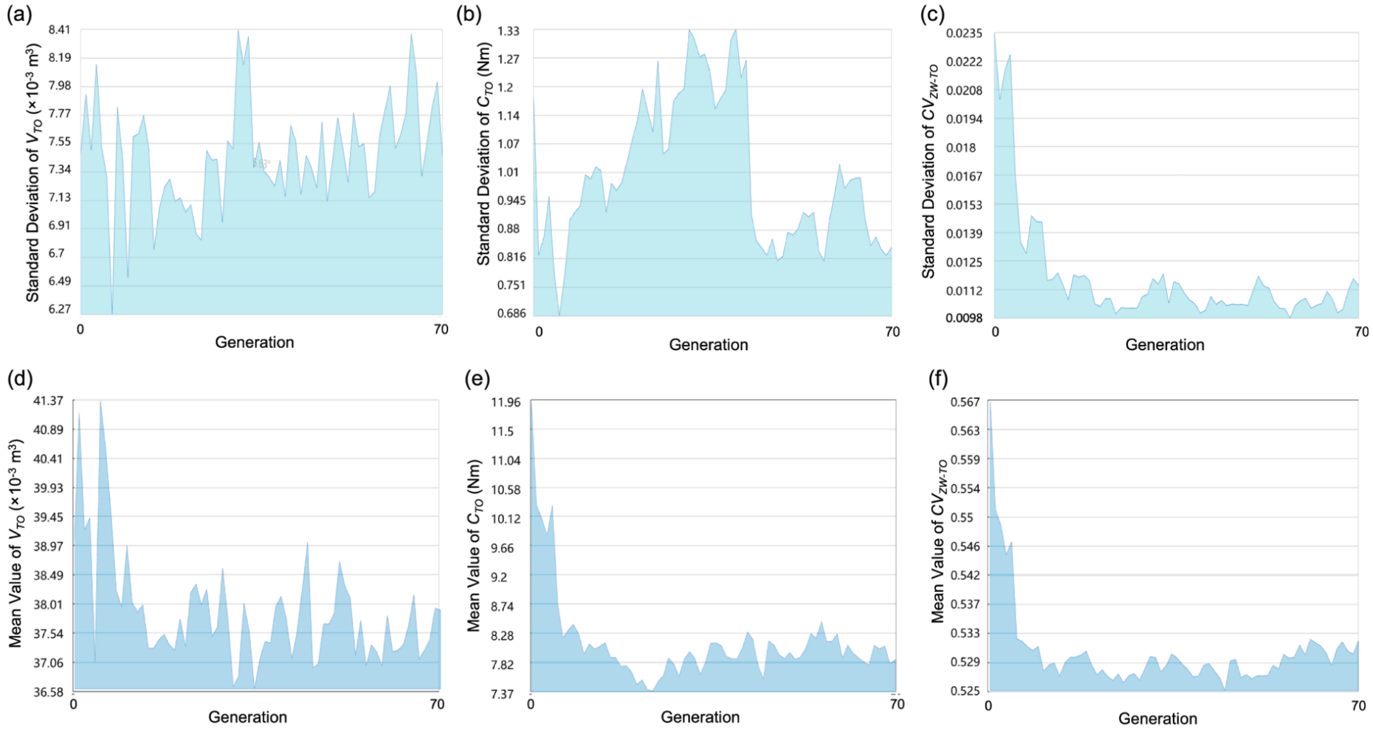

Fig. 9. Variation trends of different objectives in the multi-objective optimisation: (a-c) Variation trend of standard deviation of V_{TO}, C_{TO} and $CV_{ZW\text{-}TO}$; (d-f) Variation trend of mean value of V_{TO}, C_{TO} and $CV_{ZW\text{-}TO}$.

and actual values in the testing set. Fig. 12(b) and (d) present scatter plots of the actual versus predicted values. The deviations for most data points remain within ± 5%. The high accuracy and reliability of the BO-XGBoost models confirm their suitability for constructing robust

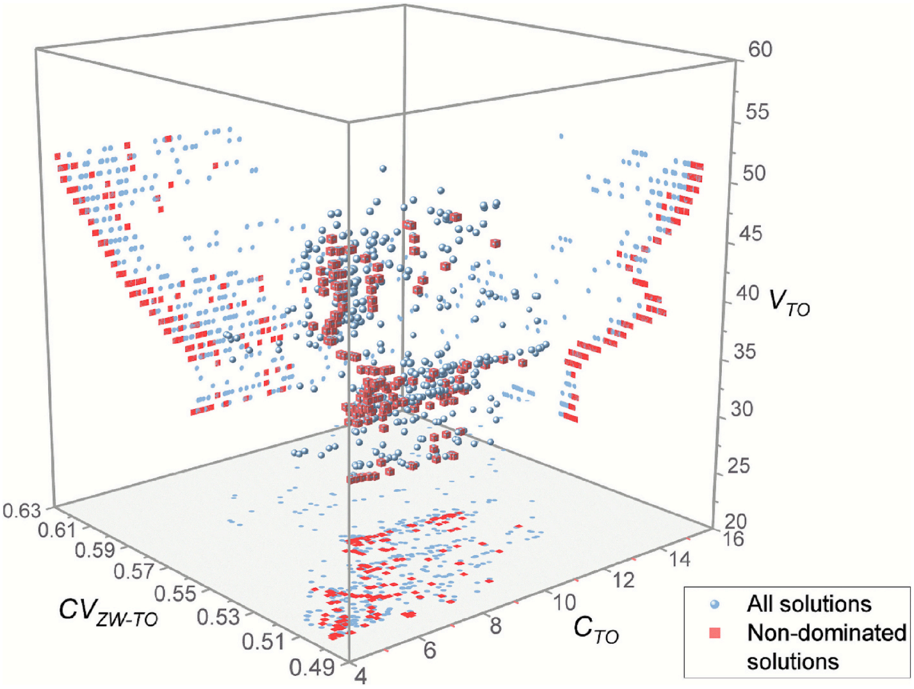

Fig. 10. Objective space of all solutions and non-dominated solutions.

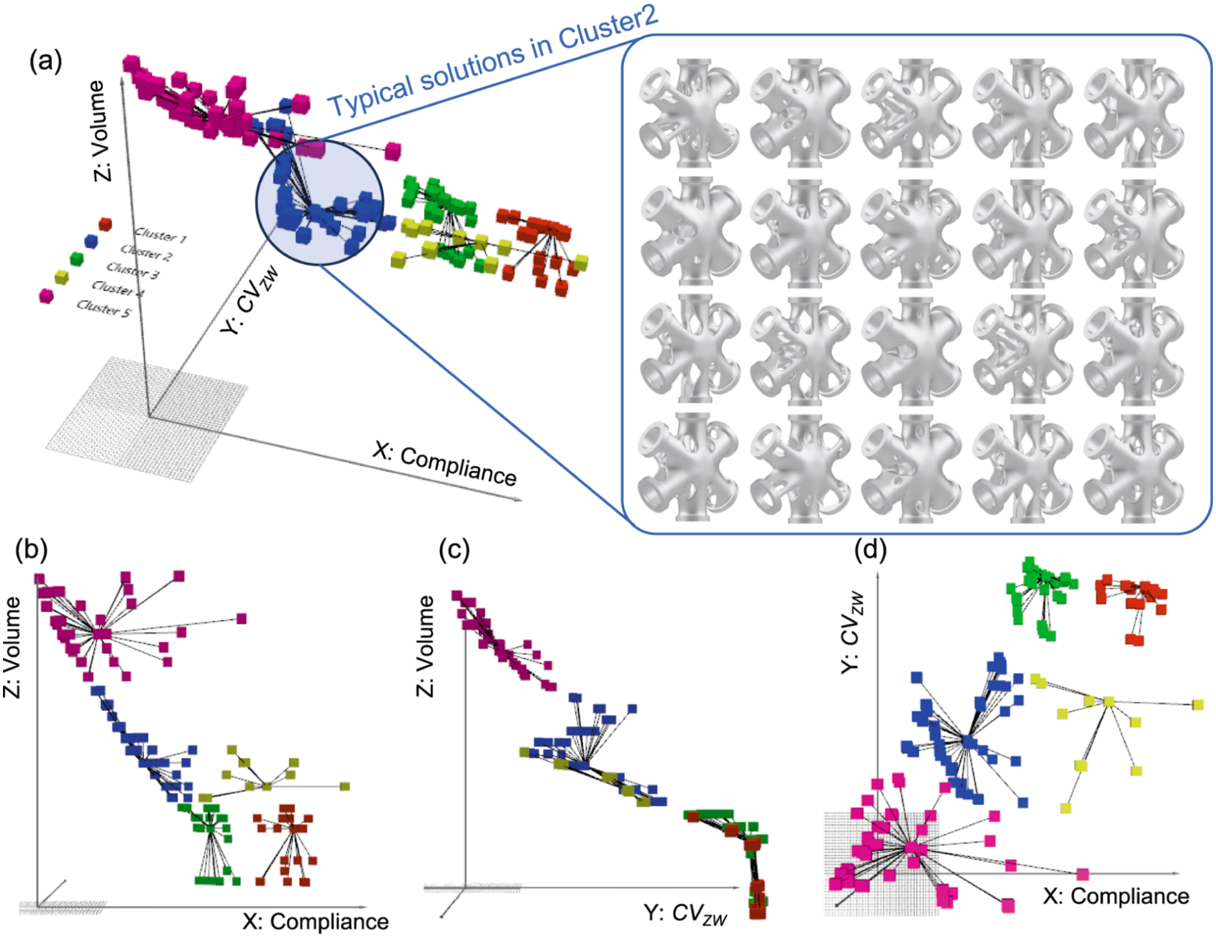

Fig. 11. Non-dominated solutions space clustered by K-means algorithm: (a) spatial distribution; (b) XZ plane; (c) YZ plane; (d) XY plane.

surrogate models for multi-objective optimisation.

Table 3
Accuracy of BO-XGBoost models.

Label	Dataset	*RMSE*	*MAE*	R^2	*MAPE*
C_{TO}	Train	0.1755	0.0633	0.9999	0.0070
	Test	0.5879	0.2262	0.9993	0.0204
CV_{ZW}	Train	0.0013	0.0007	0.9999	0.0011
	Test	0.0079	0.0025	0.9944	0.0042

5.2. Non-dominated solutions selection

By dividing the input variables and output values of all non-dominated solutions into five clusters, a parallel coordinate plot (Fig. 13) illustrates the relationships between design parameters and objective performances. The analysis reveals that LR parameters usually have relatively minimal impact on the performance objectives, as evidenced by their narrow distribution across clusters. One exception is $d_{T,1}/X_1$, which strongly influences compliance C_{TO}. Among the TO parameters, d_{mean}/S_m shows limited variation, while R_{min}/S_m and TV display broader ranges influenced by clustering. For example, clusters C1 and C3 favour lower TV, resulting in designs with higher C_{TO} and $CV_{ZW\text{-}TO}$ but reduced V_{TO}, whereas C5 adopts higher TV, leading to the opposite trend.

To evaluate the performance of the clustered non-dominated solutions and the LHS solutions, violin plots combined with histograms for each objective are plotted in Fig. 14. The interquartile range (IQR) and the 10–90% range for clustered solutions are significantly narrower than those of the LHS-TO designed joints. This indicates that clustering effectively isolates high-quality solutions, reducing variability and improving final selection efficiency. The mean fitness values of the TO designed joints based on clustered non-dominated solutions are compared with the LHS-TO designed joints, and traditional hollow spherical joints in Table 4. The subscript terms of “LHS” and “hs” in Table 4 represents the corresponding metrics for the LHS-TO designed joints and hollow spherical joints, respectively.

Cluster C5 prioritises mechanical performance at the expense of higher material usage. These joints use somewhat more material (around 24%) than the baseline LHS-TO designs but achieve far superior stiffnesses and stress distributions—compliance is roughly halved and stress variation slightly reduced compared to the baseline. This cluster exemplifies performance-optimised joints where extra material is justified by large gains in mechanical efficiency. By contrast, clusters C1 and C3 emphasise material efficiency. Joints in these clusters are lighter (20% less material than the LHS-TO baseline) while still obtaining modest performance gains. These clusters illustrate designs that sacrifice some performance (relative to C5) in exchange for weight savings. Meanwhile, cluster C2 achieves a balance between material use and mechanical performance, effectively offering an “ideal” compromise. These designs have about the same mass as the LHS-TO baseline but attain notably better performance, reducing compliance and CV_{ZW} by 44% and 8%, respectively. Every solution in cluster C2 outperforms the conventional hollow spherical joint on all objectives. A rendering of the “ideal solution” joints is illustrated in Fig. 15(a). They utilised approximately 60% of the material required for a traditional hollow spherical joint, yet the compliance and CV_{ZW} were reduced substantially, by about 42% and 67%, respectively.

The results demonstrate that K-means Clustering not only simplifies the selection of non-dominated solutions but also provides critical insights into TO designs for diverse applications. Cluster C5 is ideal for applications where material sensitivity is secondary, while clusters C1 and C3 are more appropriate for designs emphasizing material

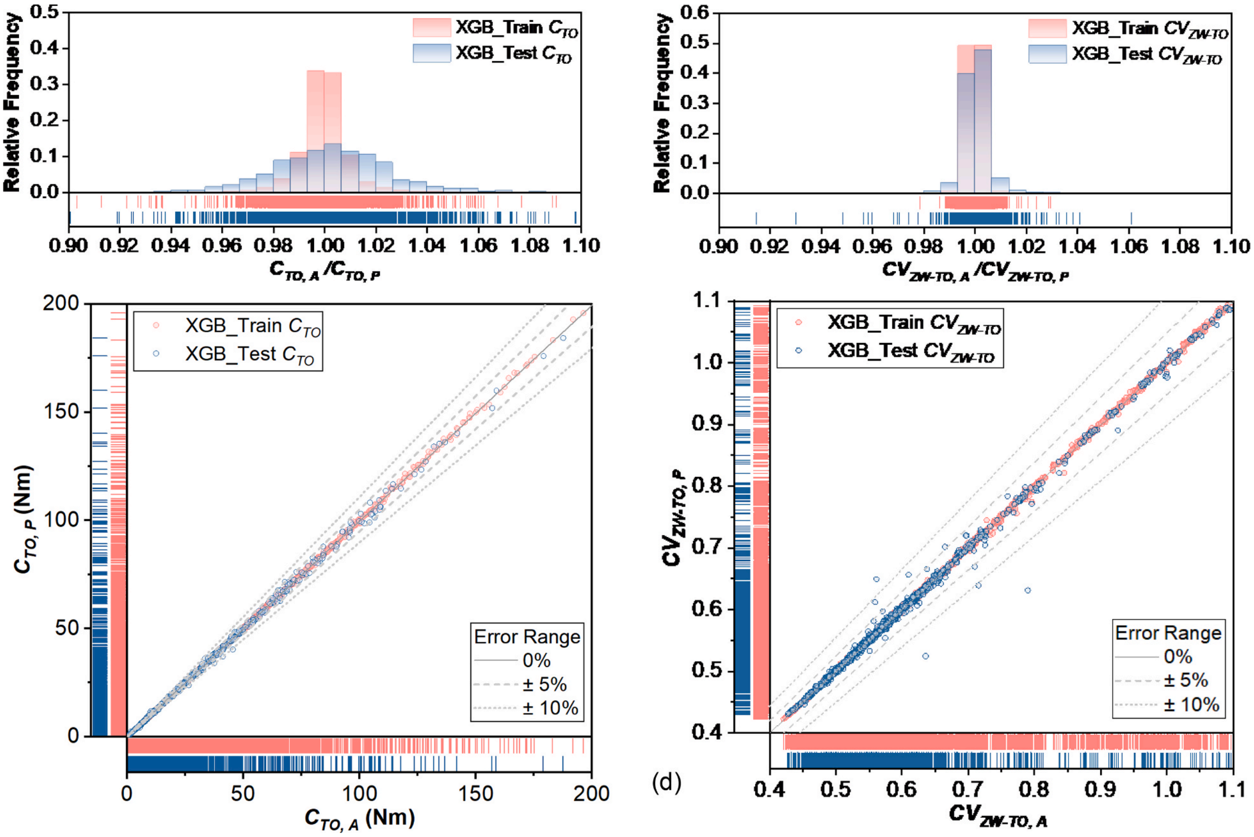

Fig. 12. BO-XGBoost model predicted values versus actual values: (a) Relative frequency histograms of the ratio between actual and predicted C_{TO} values; (b) Scatter plot of actual and predicted C_{TO} values; (c) Relative frequency histograms of the ratio between actual and predicted $CV_{ZW\text{-}TO}$ values; (d) Scatter plot of actual and predicted $CV_{ZW\text{-}TO}$ values.

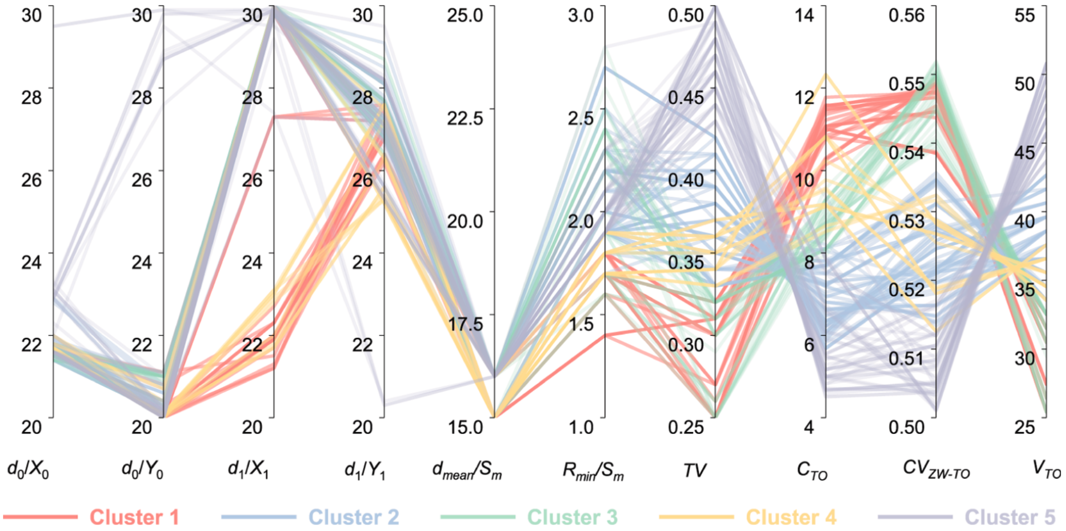

Fig. 13. Parallel coordinate plot of inputs and outputs of non-dominated solutions.

efficiency. Cluster C2, with its balanced performance, offers a practical compromise, allowing designers to achieve high-quality solutions efficiently. By integrating parametric CAD established in the TOD Module, designers can quickly generate multiple joint models (Fig. 11(a)) based on selected solutions from each cluster. These models offer a range of geometries with comparable performance and material usage, enabling further refinement based on aesthetic preferences.

5.3. Metal 3D printing manufacturing

The 3D printing process for the TO designed joint is illustrated in Fig. 15(b). First, the TO designed joint file, in.stl format, was imported into the Magics 3D Print Suite on the Materialise platform for 3D printing design. The software was used to configure the AM settings based on the machine parameters. Using the CAM module, G-code instructions were generated to guide the AM machine in fabrication. Subsequently, post-processing procedures were applied to produce the final printed product.

The imported.stl files of the TO designed joint model were scaled down to a 1:5 ratio. Through the Automatic Placement function, the model was positioned at the centre of the build platform for optimal nesting. Support structures were automatically generated to maintain the stability of the object and platform during the manufacturing process while mitigating excessive heat effects. Finally, the model, along with its support structures, was sliced into uniform layers with a thickness of 30 μm for printing. The generated G-code was then transferred to the metal 3D printer, and the joint model was fabricated using Selective Laser Melting (SLM). The process began with the deposition of stainless steel powder onto the build platform. The raw material used was 316 L stainless steel spherical powder, similar to that studied in [60,80], with a particle size range of 15 – 53 μm and a flowability of 16 s/50 g. The chemical composition of the powder is provided in Table 5. A high-energy laser beam selectively melted the powder along the planned path for the current layer. After melting, the platform was automatically lowered by the specified layer thickness, and a fresh layer of powder was deposited. This process was repeated iteratively until the joint was fully fabricated. The SLM process was conducted using an HBD-580 machine, featuring a build envelope of 250 × 250 × 250 mm. The printing parameters included a laser power of 300 W, a scanning speed of 1400 mm/s, a scanning interval of 100 μm, a layer thickness of 50 μm and a laser spot size of 80 μm.

After cooling, the printed specimen was carefully removed from the machine – Fig. 15(c) – and detached from the build platform using cutting tools. The remaining powder was cleaned, sieved, filtered and recycled for subsequent use. Support structures were then removed and the joint surfaces were polished to achieve a smooth finish. Further surface enhancement was performed using sandblasting, where high-pressure air accelerated abrasive particles onto the surface. This process improved both the cleanliness and surface roughness of the parts. Photographs of the finished product are shown in Fig. 15(d). The SLM process successfully achieved the high-fidelity fabrication of the complex TO designed joint that would be challenging to produce using conventional casting, forging or stamping methods.

6. Conclusions and future work

This study presents a novel surrogate-assisted parametric inverse design framework for the topological optimisation of steel joints suitable for 3D printing and use in gridshell structures, addressing critical challenges in joint intelligent design, performance evaluation and multi-objective trade-off. The key contributions of this work include:

(1) A unified generative inverse design framework that combines TO, ML-based mechanical performance prediction and MOO within a single parametric platform was introduced. Through this automated workflow, manual iterations were eliminated and the objectives of weight, stiffness and stress uniformity were balanced in the design of 3D-printed steel joints.
(2) A Bayesian-optimised XGBoost surrogate model, implemented as a Grasshopper plugin, was developed to predict joint mechanical performance with high accuracy ($MAPE < 3\%$). This approach accelerated design evaluation by circumventing repetitive FEA, enabling rapid evaluation and iteration in MOO.
(3) The framework was equipped with the NSGA-II algorithm and K-means clustering to identify and classify Pareto-optimal solutions. Within the resulting groups, Cluster C2 was found to balance material efficiency and both mechanical performance indices, yielding an “ideal” solution set with several aesthetically distinct variants. Relative to a conventional hollow-spherical joint, C2 designs were shown to cut material usage by more than 40% and achieve reductions of 42% in C_{TO} and 67% in $CV_{ZW\text{-}TO}$.
(4) The practical applicability of the proposed framework was confirmed through the successful manufacturing of an “ideal solution” joint using SLM 3D printing technology. This addressed the challenges associated with the manufacturability of TO designed joints, offering scalable solutions for sustainable and intelligent steel gridshell structures.

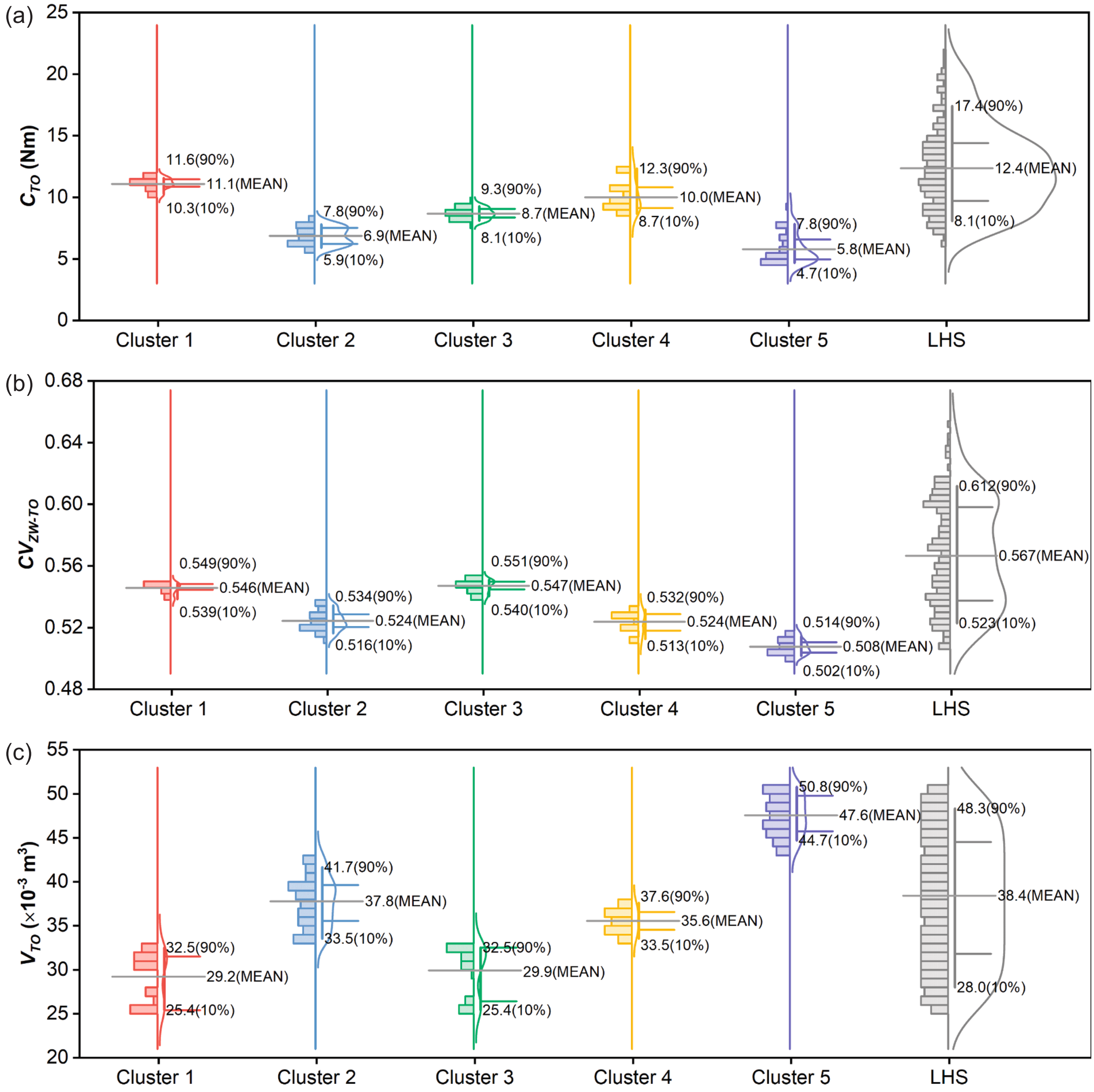

Fig. 14. Statistics of clustered non-dominated solutions and LHS solutions: (a) C_{TO}; (b) $CV_{ZW\text{-}TO}$; (c) V_{TO}.

Table 4
Mean objective metrics for clustered non-dominated TO designed joints compared with LHS-sampled TO joints and conventional hollow-spherical joints.

Series	C_{TO} (Nm)	$CV_{ZW\text{-}TO}$	V_{TO} ($\times10^{-3}$ m^3)	C_{TO}/C_{LHS}	$CV_{ZW\text{-}TO}/CV_{ZW\text{-}LHS}$	V_{TO}/V_{LHS}	C_{TO}/C_{hs}	$CV_{ZW\text{-}TO}/CV_{ZW\text{-}hs}$	V_{TO}/V_{hs}
C1-TO	11.1	0.546	29.2	0.895	0.963	0.760	0.689	0.698	0.488
C2-TO	6.9	0.524	37.8	0.556	0.924	0.984	0.429	0.670	0.632
C3-TO	8.7	0.547	29.9	0.702	0.965	0.779	0.540	0.699	0.500
C4-TO	10.0	0.524	35.6	0.806	0.924	0.927	0.621	0.670	0.595
C5-TO	5.8	0.508	47.6	0.468	0.896	1.240	0.360	0.650	0.796
LHS-TO	12.4	0.567	38.4	–	–	–	0.770	0.725	0.642

Future research will focus on expanding and refining the parametric inverse design framework to address emerging challenges and broaden its applicability. Future studies could incorporate manufacturability metrics (e.g., minimising support material, reducing overhang angles, or simplifying geometries for fabrication) as additional objectives or constraints. Additionally, efforts will be made to generalise the framework to accommodate various joint types and structural systems, ensuring its adaptability and applicability across a wide range of architectural and engineering contexts. These advancements aim to support the broader adoption of TO designed joints, driving innovation in sustainable and intelligent construction practices.

CRediT authorship contribution statement

Man-Tai Chen: Writing – original draft, Investigation, Funding acquisition, Conceptualization. **Yue Pan:** Writing – review & editing,

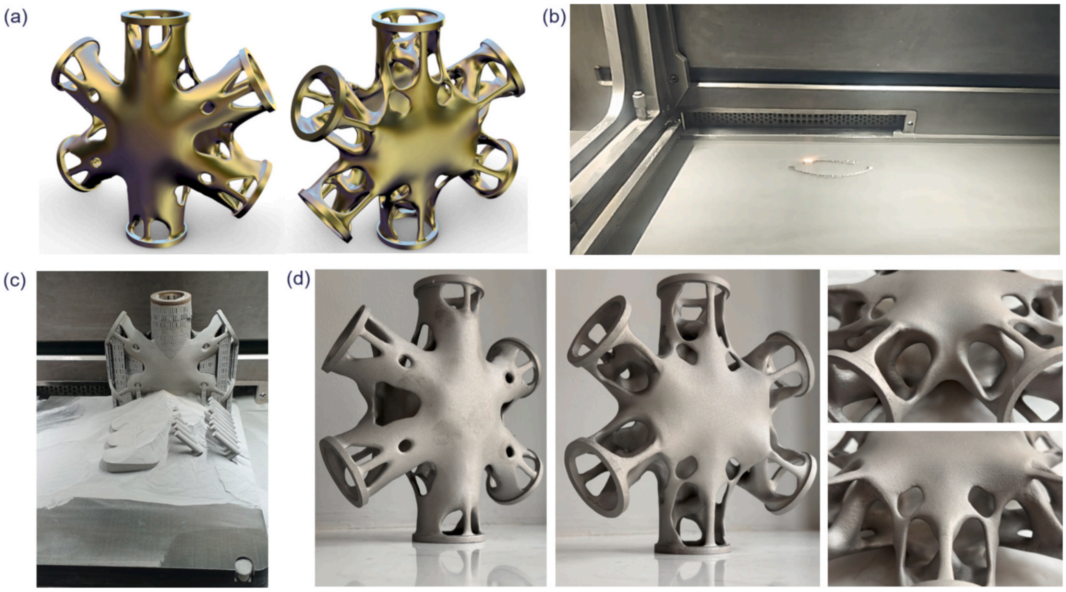

Fig. 15. Metal 3D printing of optimised joint: (a) Rendering of "ideal solution" joint model; (b) SLM processes; (c) Printing result; (d) Photos of post-processed joint.

Table 5
Chemical composition of the 316 L stainless steel feedstock powder in % by weight, with Fe making up the remainder.

C	Si	Cr	Ni	Mn	Mo	Cu	S	P	O
≤0.03	≤1.0	16–18	10–14	≤2.0	2.0–3.0	0.15–0.25	≤0.03	≤0.045	≤0.08

Methodology, Investigation. **Wenkang Zuo:** Writing – original draft, Software, Formal analysis, Conceptualization. **Ou Zhao:** Validation, Supervision. **Leroy Gardner:** Writing – review & editing, Supervision.

Declaration of competing interest

The authors declare that they have no known competing financial interests or personal relationships that could have appeared to influence the work reported in this paper.

Acknowledgements

The authors gratefully acknowledge the financial support provided by the National Natural Science Foundation of China (No. 52378167), and the Shanghai Rising-Star Program, China (No. 24QA2704400).

Data availability

Data will be made available on request.

References

[1] M.T. Chen, W. Zuo, B. Young, Tests of cold-formed steel T-joints with semi-oval hollow section chord, J. Struct. Eng. 149 (8) (2023) 04023099.
[2] I.M. de Oliveira, R.M.D.O. Pauletti, L.C. Meneghetti, Connection system for gridshell structures using parametric modeling and digital fabrication, Autom. Constr. 109 (2020) 102996.
[3] H. Chang, X. Yan, W. Zuo, J. Xia, T. Yu, Numerical analysis and design methods of grout-filled GFRP tube repaired corroded CHS T-joints, Thin-Walled Struct. 198 (2024) 111719.
[4] SS Song, J Chen, F Xu, Mechanical behaviour and design of concrete-filled K and KK CHS connections, Journal of Constructional Steel Research 188 (2022) 107000.
[5] W. Zuo, H. Chang, Z. Li, A. An, J. Xia, T. Yu, Experimental investigation on compressive behavior of corroded thin-walled CHS T-joints with grout-filled GFRP tube repairing, Thin-Walled Struct. 175 (2022) 109222.
[6] X. Yan, W. Zuo, Z. Li, J. Xia, H. Chang, Design rule of grout-filled GFRP tube repaired corroded CHS X-joints, J. Constr. Steel Res. 235 (2025) 109792.
[7] H. Chang, W. Zuo, J. Yang, X. Song, Y. Huang, Compressive strength of collar plate reinforced SHS T-joints: effect of geometrical parameters and chord stress ratio, J. Constr. Steel Res. 174 (2020) 106278.
[8] H. Chang, W. Zuo, J. Xia, B. Xu, R. Ma, L.H. Zhang, Sensitivity analysis of geometrical design parameters on the compressive strength of the vertical inner-plate reinforced square hollow section T-joints: a finite element study, Eng. Struct. 208 (2020) 110308.
[9] B. Cheng, F. Huang, Y. Duan, M.T. Chen, Fatigue performance of bird-beak SHS gap K-joints under brace in-plane force, J. Struct. Eng. 147 (11) (2021) 04021167.
[10] X. Huang, Y.M. Xie, Convergent and mesh-independent solutions for the bi-directional evolutionary structural optimization method, Finite Elem. Anal. Des. 43 (14) (2007) 1039–1049.
[11] X. Huang, Y.M. Xie, Bi-directional evolutionary topology optimization of continuum structures with one or multiple materials, Comput. Mech. 43 (3) (2009) 393–401.
[12] J. Lange, T. Feucht, M. Erven, 3D printing with steel additive manufacturing for connections and structures, Steel Constr. Des. Res. 13 (3) (2020) 144–153.
[13] P. Block, J. Knippers, N.J. Mitra, W. Wang, New Opportunities to Optimize Structural designs in Metal by using Additive Manufacturing, Springer International Publishing AG, Switzerland, 2015.
[14] Galjaard S, Hofman S, Perry N, Ren S. Optimizing structural building elements in metal by using additive manufacturing. In: Proceedings of the International Association for Shell and Spatial Structures (IASS), Symposium 2015, 17 - 20 August 2015, Amsterdam, The Netherlands.
[15] V. Hassani, Z. Khabazi, H.A. Mehrabi, C. Gregg, R.W. O'Brien, Rationalization algorithm for a topologically-optimized multi-branch node for manufacturing by metal printing, J. Build. Eng. 29 (2020) 101146.
[16] T.P. Ribeiro, L.F.A. Bernardo, J.M.A. Andrade, Topology optimisation in structural steel design for additive manufacturing, Appl. Sci. 11 (5) (2021) 2112.
[17] M.T. Chen, W. Zuo, Y. Chen, O. Zhao, B. Cheng, J. Zhao, Parametric topology optimization design and analysis of additively manufactured joints in spatial grid structures, Eng. Struct. 300 (2024) 117123.
[18] X. Meng, L. Gardner, Hybrid construction featuring wire arc additive manufacturing review, concepts, challenges and opportunities, Eng. Struct. 326 (2025) 119337.
[19] Z. Wang, Y. Hou, M.T. Chen, F. Xu, X. Yun, Optimization and testing of wire arc additively manufactured steel tubular T-joints, J. Struct. Eng. 152 (2) (2026) 04025254.
[20] M.T. Chen, T. Zhang, Z. Gong, W. Zuo, Z. Wang, L. Zong, O. Zhao, L. Hu, Mechanical properties and microstructure characteristics of wire arc additively manufactured high-strength steels, Eng. Struct. 300 (2024) 117092.
[21] X. Meng, B. Weber, M. Nitawaki, L. Gardner, Optimisation and testing of wire arc additively manufactured steel stub columns, Thin-Walled Struct. 189 (2023) 110857.

[22] M.T. Chen, Z. Gong, T. Zhang, W. Zuo, Y. Zhao, O. Zhao, G. Zhang, Z. Wang, Mechanical behavior of austenitic stainless steels produced by wire arc additive manufacturing, Thin-Walled Struct. 196 (2024) 111455.

[23] M.T. Chen, Y. Chen, W. Zuo, X. Yun, O. Zhao, S.W. Liu, F. Xu, Experimental investigation on the tensile behavior of wire arc additively manufactured duplex stainless steel plates, Eng. Struct. 321 (2024) 118764.

[24] B. Weber, X. Meng, R. Zhang, M. Nitawaki, T. Sagawa, L. Gardner, Tensile behaviour of WAAM high strength steel material and members, Mater. Des. 237 (2024) 112517.

[25] P. Kyvelou, A. Spinasa, L. Gardner, Testing and analysis of optimized wire arc additively manufactured steel trusses, J. Struct. Eng. 150 (3) (2024) 04024008.

[26] L. Gardner, Metal additive manufacturing in structural engineering-review, advances, opportunities and outlook, Structures 47 (2023) 2178–2193.

[27] A. Kanyilmaz, A.G. Demir, M. Chierici, F. Berto, L. Gardner, S.Y. Kandukuri, P. Kassabian, T. Kinoshita, A. Laurenti, I. Paoletti, A. du Plessis, S.M.J. Razavi, Role of metal 3D printing to increase quality and resource-efficiency in the construction sector, Addit. Manuf. 50 (2022) 102541.

[28] L. Gardner, J. Li, X. Meng, C. Huang, P. Kyvelou, I-section steel columns strengthened by wire arc additive manufacturing - concept and experiments, Eng. Struct. 306 (2024) 117763.

[29] X. Meng, L. Gardner, Standardisation framework for metal additive manufacturing in construction, Autom. Constr. 176 (2025) 106267.

[30] D. Yang, D. Di Stefano, M. Turrin, S. Sariyildiz, Y. Sun, Dynamic and interactive re-formulation of multi-objective optimization problems for conceptual architectural design exploration, Autom. Constr. 118 (2020) 103251.

[31] J. Wang, K. Chen, H. Yang, L. Zhang, Ensemble deep learning enabled multi-condition generative design of aerial building machine considering uncertainties, Autom. Constr. 157 (2024) 105134.

[32] X. Wang, Y. Pan, M.G. Li, J.J. Chen, A novel data-driven optimization framework for unsupervised and multivariate early-warning threshold modification in risk assessment of deep excavations, Expert Syst. Appl. 238 (2024) 121872.

[33] Y. Pan, L.M. Zhang, Mitigating tunnel-induced damages using deep neural networks, Autom. Constr. 138 (2022) 104219.

[34] K. Liu, X. Xu, W. Huang, R. Zhang, L. Kong, X. Wang, A multi-objective optimization framework for designing urban block forms considering daylight, energy consumption, and photovoltaic energy potential, Build. Environ. 242 (2023) 110585.

[35] K. Guo, L. Zhang, Multi-objective optimization for improved project management: current status and future directions, Autom. Constr. 139 (2022) 104256.

[36] P. Qu, L. Zhang, Uncertainty-based multi-objective optimization in twin tunnel design considering fluid-solid coupling, Reliab. Eng. Syst. Saf. 253 (2025) 110575.

[37] Y. Pan, Y. Shen, J. Qin, L. Zhang, Deep reinforcement learning for multi-objective optimization in BIM-based green building design, Autom. Constr. 166 (2024) 105598.

[38] Xie YM. Generalized Topology Optimization for Structural Design, Springer Nature, 2025.

[39] L. Wang, W. Du, P. He, M. Yang, Topology optimization and 3D printing of three-branch joints in treelike sructures, J. Struct. Eng. 146 (1) (2020) 04019167.

[40] W. Zuo, M.T. Chen, Y. Chen, O. Zhao, B. Cheng, J. Zhao, Additive manufacturing oriented parametric topology optimization design and numerical analysis of steel joints in gridshell structures, Thin-Walled Struct. 188 (2023) 110817.

[41] Y. Han, W. Du, Q. Wang, H. Xue, B. Gao, S. Dong, Generation of innovative structural connection components using generative adversarial networks, Adv. Eng. Inf. 68 (2025) 103608.

[42] W. Du, Y. An, H. Xue, B. Gao, S. Dong, Generation and evaluation of unimaginable three-dimensional structural joints using generative adversarial networks, Autom. Constr. 167 (2024) 105707.

[43] S. Ren, S. Galjaard, Topology Optimisation for Steel Structural Design with Additive Manufacturing, Springer International Publishing, 2015.

[44] H. Seifi, A.R. Javan, S.Q. Xu, Y. Zhao, Y.M. Xie, Design optimization and additive manufacturing of nodes in gridshell structures, Eng. Struct. 160 (2018) 161–170.

[45] V. Laghi, N. Babovic, E. Benvenuti, H. Kloft, Blended structural optimization of steel joints for Wire-and-Arc Additive Manufacturing, Eng. Struct. 300 (2024) 117141.

[46] W. Zuo, M.T. Chen, O. Zhao, L. Gardner, Testing of wire arc additively manufactured duplex stainless steel double-lap shear bolted connections, J. Struct. Eng. 151 (2) (2025) 04024205.

[47] W. Zuo, M.T. Chen, S.W. Liu, X. Yun, O. Zhao, Y. Huang, B. Cheng, Experimental investigation on double-lap shear behavior of 3D printed austenitic stainless steel bolted connections, Eng. Struct. 317 (2024) 118501.

[48] W. Zuo, M.T. Chen, O. Zhao, A.D. Su, S.W. Liu, X. Yun, F.D. Xu, Structural performance of wire arc additively manufactured duplex stainless steel single-lap shear bolted connections, Eng. Struct. 319 (2024) 118706.

[49] W. Zuo, M.T. Chen, O. Zhao, A.D. Su, S.W. Liu, F. Xu, Y. Huang, B. Cheng, Behavior of wire arc additively manufactured 316L austenitic stainless steel single shear bolted connections, Thin-Walled Struct. 202 (2024) 112075.

[50] I.H. Shah, N. Hadjipantelis, L. Walter, R.J. Myers, L. Gardner, Environmental life cycle assessment of wire arc additively manufactured steel structural components, J. Clean. Prod. 389 (2023) 136071.

[51] X. Guo, P. Kyvelou, J. Ye, L.H. Teh, L. Gardner, Experimental investigation of wire arc additively manufactured steel single-lap shear bolted connections, Thin-Walled Struct. 181 (2022) 110029.

[52] B. Weber, X. Meng, L. Gardner, An optimised and 3D printed steel garden bridge – from design to experimental verification, Autom. Constr. 181 (2026) 106638.

[53] Z.C. Gong, H.T. Li, W. Chen, O. Zhao, M.T. Chen, Material properties of wire arc additively manufactured austenitic stainless steels after exposure to elevated temperatures, Thin-Walled Struct. 211 (2025) 113061.

[54] Z.C. Gong, H.T. Li, W. Chen, O. Zhao, M.T. Chen, Post-fire tensile behavior of wire arc additively manufactured duplex stainless steel plates, Eng. Struct. 343 (2025) 120800.

[55] Y.Y. Chen, M.T. Chen, O. Zhao, B. Rossi, X.F. Ruan, Fatigue crack growth behavior of wire arc additively manufactured 316L austenitic stainless steel, Thin-Walled Struct. 212 (2025) 113182.

[56] Y.Y. Chen, M.T. Chen, O. Zhao, C. Huang, L. Gardner, Fatigue crack growth in wire arc additively manufactured ER2594 super-duplex stainless steel - testing and modelling, Eng. Struct. 343 (2025) 120912.

[57] M.T. Chen, Y.Y. Chen, C. Huang, L. Gardner, O. Zhao, Experimental investigation of fatigue crack growth in wire arc additively manufactured ER2209 duplex stainless steel, J. Constr. Steel Res. 231 (2025) 109615.

[58] C. Huang, P. Kyvelou, L. Gardner, Stress-strain curves for wire arc additively manufactured steels, Eng. Struct. 279 (2023) 115628.

[59] C. Huang, L. Li, N. Pichler, E. Ghafoori, L. Susmel, L. Gardner, Fatigue testing and analysis of steel plates manufactured by wire-arc directed energy deposition, Addit. Manuf. 73 (2023) 103696.

[60] R. Zhang, M. Amraei, H. Piili, L. Gardner, Microstructure, mechanical properties and cross-sectional behaviour of additively manufactured stainless steel cylindrical shells, Thin-Walled Struct. 208 (2025) 112750.

[61] R. Zhang, X. Meng, L. Gardner, Shape optimisation of stainless steel corrugated cylindrical shells for additive manufacturing, Eng. Struct. 270 (2022) 114857.

[62] J.J. Yan, M.T. Chen, W.M. Quach, M. Yan, B. Young, Mechanical properties and cross-sectional behavior of additively manufactured high strength steel tubular sections, Thin-Walled Struct. 144 (2019) 106158.

[63] M. Chierici, F. Berto, A. Kanyilmaz, Resource-efficient joint fabrication by welding metal 3D-printed parts to conventional steel: a structural integrity study, Fat. Fract. Eng. Mater. Struct. 44 (5) (2021) 1271–1291.

[64] A. Kanyilmaz, F. Berto, I. Paoletti, R.J. Caringal, S. Mora, Nature-inspired optimization of tubular joints for metal 3D printing, Struct. Multidiscip. Optim. 63 (2) (2021) 767–787.

[65] S.B. Huang, X.W. Deng, Experiments and investigation of planar high-strength steel joints with Additive Manufacturing, Thin-Walled Struct. 200 (2024) 111887.

[66] S.B. Huang, X.W. Deng, L.K. Lam, Integrated design framework of 3D printed planar stainless tubular joint: Modelling, optimization, manufacturing, and experiment, Thin-Walled Struct. 169 (2021) 108463.

[67] S.B. Huang, X.W. Deng, Y.H. Wang, Experimental investigations of optimized 3D printing planar X-joints manufactured by stainless steel and high-strength steel, Eng. Struct. 285 (2023) 116054.

[68] Chen T, Guestrin C. XGBoost: A scalable tree boosting system. In: Proceedings of the 22nd ACM SIGKDD International Conference on Knowledge Discovery and Data Mining, August 13-17, 2016, San Francisco, CA, USA; 785–794.

[69] Y. Shen, Y. Pan, BIM-supported automatic energy performance analysis for green building design using explainable machine learning and multi-objective optimization, Appl. Energy 333 (2023) 120575.

[70] K. Deb, A. Pratap, S. Agarwal, T. Meyarivan, A fast and elitist multiobjective genetic algorithm: NSGA-II, IEEE Trans. Evol. Comput. 6 (2) (2002) 182–197.

[71] E. Catmull, J. Clark, Recursively generated B-spline surfaces on arbitrary topological meshes, Comput. Aided Des. 10 (6) (1978) 350–355.

[72] K. Museth, VDB: High-resolution sparse volumes with dynamic topology, ACM Trans. Graph. 32 (3) (2013) 27.

[73] Huang J, Zhou Y, Niessner M, Shewchuk J, Guibas L. QuadriFlow: A Scalable and Robust Method for Quadrangulation. Eurographics Symposium on Geometry Processing 2018;37(5):147–160.

[74] W. Zuo, M.T. Chen, B. Young, Post-fire behavior of cold-formed steel semi-oval hollow stub columns, J. Struct. Eng. 150 (10) (2024) 04024141.

[75] W. Zuo, M.T. Chen, B. Young, Structural behaviour of cold-formed steel elliptical hollow section stub columns after exposure to ISO-834 fire curve, Thin-Walled Struct. 197 (2024) 111309.

[76] CIDECT Design Guide No. 1. Design guide for circular hollow section (CHS) joints under predominantly static loading. Geneva, Switzerland: CIDECT; 2008.

[77] S. Hu, W. Wang, X. Lin, Two-stage machine learning framework for developing probabilistic strength prediction models of structural components: an application for RHS-CHS T-joint, Eng. Struct. 266 (2022) 114548.

[78] S.-H. Kim, X. Song, C. Cho, C.-H. Lee, Strength prediction of steel CHS X-joints via leveraging finite element method and machine learning solutions, J. Constr. Steel Res. 176 (2021) 106394.

[79] N.-H. Nguyen, K.T. Tong, S. Lee, A. Karamanli, T.P. Vo, Prediction compressive strength of cement-based mortar containing metakaolin using explainable Categorical Gradient Boosting model, Eng. Struct. 269 (2022) 114768.

[80] W.K. Zuo, M.T. Chen, O. Zhao, L. Gardner, Parametric optimization design and testing of 3D printed stainless steel circular X-joints, Eng. Struct. 353 (2026) 122148.